

Effect of strike point displacements on the ITER tungsten divertor heat loads

*Original*

Effect of strike point displacements on the ITER tungsten divertor heat loads / Carli, S.; Pitts, R. A.; Bonnin, X.; Subba, F.; Zanino, R.. - In: NUCLEAR FUSION. - ISSN 0029-5515. - 58:12(2018), p. 126022. [10.1088/1741-4326/aae43f]

*Availability:*

This version is available at: 11583/2781256 since: 2020-01-16T16:12:00Z

*Publisher:*

Institute of Physics Publishing

*Published*

DOI:10.1088/1741-4326/aae43f

*Terms of use:*

This article is made available under terms and conditions as specified in the corresponding bibliographic description in the repository

*Publisher copyright*

(Article begins on next page)

PAPER • OPEN ACCESS

## Effect of strike point displacements on the ITER tungsten divertor heat loads

To cite this article: S. Carli *et al* 2018 *Nucl. Fusion* **58** 126022

View the [article online](#) for updates and enhancements.

### Recent citations

- [Dynamics of neon ions after neon gas seeding into tokamak plasma](#)  
N. Bisai *et al*



**IOP | ebooks™**

Bringing you innovative digital publishing with leading voices to create your essential collection of books in STEM research.

Start exploring the collection - download the first chapter of every title for free.

# Effect of strike point displacements on the ITER tungsten divertor heat loads

S. Carli<sup>1</sup>, R.A. Pitts<sup>2</sup>, X. Bonnin<sup>2</sup>, F. Subba<sup>3</sup> and R. Zanino<sup>3</sup>

<sup>1</sup> Department of Mechanical Engineering, KU Leuven, Celestijnenlaan 300, 3001 Leuven, Belgium

<sup>2</sup> ITER Organization, Route de Vinon sur Verdon, CS 90 046, 13067 Saint Paul Lez Durance Cedex, France

<sup>3</sup> NEMO Group, Dipartimento Energia, Politecnico di Torino, Corso Duca degli Abruzzi 24, 10129 Torino, Italy

E-mail: [stefano.carli@kuleuven.be](mailto:stefano.carli@kuleuven.be)

Received 4 June 2018, revised 13 September 2018

Accepted for publication 26 September 2018

Published 11 October 2018



CrossMark

## Abstract

The baseline ITER burning plasma equilibrium is designed to place the divertor strike points deep into the ‘V-shaped’ region formed by the high heat flux handling vertical targets (VT) and the reflector plates (RP). The divertor plasma performance under these conditions has been extensively studied in the past two decades with the SOLPS4.3 plasma boundary code suite. However, during tokamak operation, inaccuracies in the control of the vertical plasma position, or a requirement to avoid damaged monoblocks, could force the strike point position further down the VTs, or even directly on the RPs. In this paper, we present the results from the first SOLPS-ITER modelling in which the consequences of strike point displacements on the divertor plasma behaviour and surface heat loading are assessed. The starting point of the study is a baseline coupled fluid plasma-kinetic neutral solution (without fluid drifts), corresponding to an ITER burning plasma scenario at  $Q_{DT} = 10$  with neon seeding for detachment control,  $P_{SOL} = 100$  MW,  $\lambda_q \sim 2$  mm and nominal strike point positions. From this baseline condition, the equilibrium is progressively moved downwards in a series of rigid displacements, obtaining new steady-state solutions, up to a maximum displacement of  $\sim 8$  cm, beyond which the separatrix is too close to the inner dome wing. At this point, the inner strike point is well onto the inner RP while the outer strike point is still on the VT. The different interaction of the recycled neutrals with the SOL plasma when the strike point intersects the inner RP, switching from vertical to horizontal target configuration, enhances the detachment degree at the inboard divertor, mitigating the heat load deposited onto the inner RP. At the outboard divertor the plasma condition is not significantly affected by the downward displacements, nor are the power fluxes to the outer RP. Finally, the heat load profiles computed with SOLPS are used in input for a finite element thermal analysis, considering the full cooling geometry, to assess the response of the VTs and RPs under the conditions exploited in the displaced scenarios. This thermal model, based on a simplified treatment not requiring a full 3D description of the divertor monoblock plasma-facing units, constitutes a new module for the SOLPS-ITER code suite.

Keywords: ITER, divertor, power exhaust, detachment, SOLPS-ITER

(Some figures may appear in colour only in the online journal)



Original content from this work may be used under the terms of the [Creative Commons Attribution 3.0 licence](https://creativecommons.org/licenses/by/3.0/). Any further distribution of this work must maintain attribution to the author(s) and the title of the work, journal citation and DOI.

## 1. Introduction

The ITER divertor is a key component, providing the principal heat exhaust channel, maintaining acceptable core impurity levels and ensuring adequate particle exhaust for the control of the helium ash during burning plasma operation [1]. It has been the subject of very careful physics design over a period of two decades (see e.g. [2–8]) and is now entering the procurement phase.

The divertor configuration is shown in figure 1(a) [1], where the main plasma-facing components (PFC) are identified. The vertical targets (VTs), comprising rows of plasma-facing units (PFU) each consisting of discrete tungsten (W) monoblocks bonded onto copper–chromium–zirconium (CuCrZr) cooling tubes, are capable of handling stationary heat loads up to 10 MW m<sup>-2</sup>. The reflector plates (RPs) and the dome are made of W flat tiles bonded to a CuCrZr heat sink with hypervapotron cooling technology [9]. They can handle stationary loads of 5 MW m<sup>-2</sup> and excursions up to 10 MW m<sup>-2</sup> for a few seconds. The function of the RPs is to protect the cassette body (CB) from plasma radiation and downwards strike point movements, while the dome plays the important role of improving the confinement of neutral particles with the added beneficial effect on throughput, enhancing He exhaust [7]. It also offers a moderate degree of neutron screening for the lower part of the vacuum vessel.

During baseline operation of ITER at  $Q_{DT} = 10$ , the power  $P_{SOL}$  that will cross the separatrix entering the scrape-off layer (SOL) can be roughly estimated as 100 MW. About 90% of this power must be exhausted within the divertor. Under these conditions, the only way to maintain divertor target heat fluxes below the technologically allowed limits is to use an extrinsic impurity, e.g. neon (Ne) to volumetrically dissipate the plasma thermal power flowing parallel to the magnetic field in the divertor target region. This dissipation ensures partial detachment of the thermal flux on the target in the strike point vicinity, where the parallel power flow is highest. Depending on the operating point, plasma boundary simulations (similar to those described in this paper) typically find that between 50–65 MW of power must be radiated in the divertor volume (including contributions from impurity and hydrogenic radiation) to satisfy the target power handling requirements. The ITER divertor makes use of a vertical target configuration to promote detachment, with strike points nominally placed low down on the targets deep into the ‘V-shaped’ region formed by the VTs and the RPs (see figure 1(b)).

The divertor plasma behaviour and VT heat loading in different operating conditions have been extensively studied during the past years using the SOLPS4.3 code package, see e.g. [10] for burning plasma conditions and [11] for lower power operation. Conversely, for the RPs the only detailed study carried out so far has focussed on the heat loading from photons in a highly radiative divertor [12], showing that the maximum heat flux on the plates is typically lower than 1 MW m<sup>-2</sup>. However, during tokamak operation, the strike points can move from their baseline location due to inaccuracies in the control of the vertical plasma position or may need to be permanently displaced in order to avoid damaged

regions of the targets. As shown in a previous analysis with the SOLPS-4.2 code [13], upward displacements may be problematic due to weaker pumping, whilst downward movements, if they are sufficiently large, could even result in strike point excursions onto the RP, particularly at the inner divertor. Past experiments and modelling studies have addressed the effect of different divertor geometries in tokamaks like JET, AUG and JT-60U [14]. However, the heat load conditions and divertor plasma behaviour as the strike points are lowered have never been assessed quantitatively for ITER. This paper aims to provide such an assessment, with findings that are in good agreement with those obtained in [14].

The paper is organized as follows: in section 2 the setup for the SOLPS-ITER simulations is described; in section 3 the simplified heat transfer model for the ITER PFC developed here is described; in section 4 the results of the SOLPS-ITER simulations as well as of the simplified heat transfer model are shown and discussed; in section 5 conclusions on the work are drawn.

## 2. SOLPS-ITER simulation setup

The SOLPS-ITER code suite [15, 16], comprising the B2.5 plasma fluid code and the EIRENE Monte Carlo neutral kinetic code, has been adopted to perform the steady-state plasma-edge simulations reported here. SOLPS-ITER is the successor to the SOLPS4.3 package used extensively to guide the design of the ITER divertor. The main differences between their physics and numerical models, as described in [15, 17], are in the plasma solver, with SOLPS-ITER adopting the most recent version B2.5 which includes drifts and currents, and the most recent version of the Monte Carlo EIRENE code for the neutral transport, with a wide set of neutral–neutral collisions. The two codes were benchmarked against each other in [15], showing good general agreement but with some deviations in the cases at higher power and low throughput, where SOLPS-ITER predicts up to a factor 2 higher heat flux density at the outer target. Efforts are still underway to identify the origins of these discrepancies, though they are thought to be a major issue, particularly in view of the expected operation point of the divertor at high fusion performance, where high throughput (high sub-divertor neutral pressure) will be mandatory to maintain target heat flux densities below technologically feasible levels.

A plot of the computational domains and meshes for B2.5 and EIRENE is shown in figure 2. The B2.5 grid adopted consists of 90 cells in the poloidal direction and 36 in the radial direction, similar to the choices made for other studies [18]. The divertor region in particular has been modelled with 20 poloidal cells up to the X-point for each divertor leg, while in the radial direction the SOL region is discretized with 28 cells (with 8 in the private flux region (PFR)).

Starting from a magnetic equilibrium corresponding closely (within ~1 cm) to the nominal strike point positions assumed in the extensive SOLPS-4.3 scoping studies performed for the ITER divertor baseline design, the equilibrium has been rigidly moved downward in a series of 2 cm displacements, up

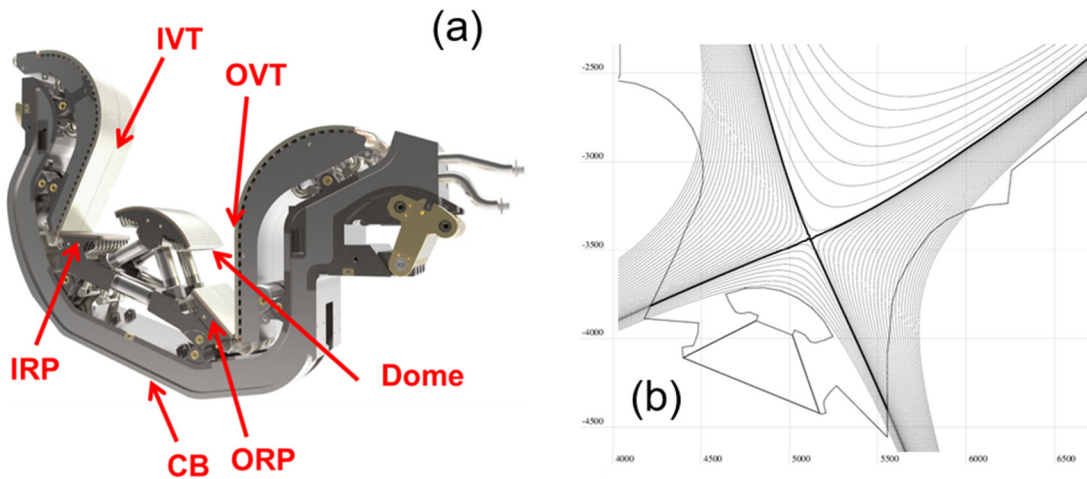


**Figure 1.** (a) Current ITER divertor design. ‘I’ denotes inner and ‘O’ denotes outer. See main text for definition of the various component names. Reprinted from [8], Copyright 2018, with permission from ITER Organization. Published by Elsevier B.V. All rights reserved. (b) Baseline,  $q_{95} = 3$  magnetic equilibrium reconstruction in the divertor region showing the nominal separatrix position and the wall surface model used in the SOLPS-ITER simulations.

to a maximum of 8 cm, see figure 3. Further displacements, in principle up to  $\sim 10$  cm beyond this value could be obtained, at which the separatrix is a few mm from intersecting the inner dome wing. However, we limit the study to the maximum displacement of 8 cm since a separatrix position too close to the dome would in practice be avoided in anything but off-normal situations due to the risk of power overload. In addition, the inner dome wing is the limiting structure for the B2.5 computational domain and, as the separatrix approaches it, the PFR reduces in extent, to the point at which it becomes too close to the decay length boundary condition applied there, see below. From the plot of the total strike point angle in figure 4(a) (which takes into account the monoblock top surface (toroidal bevel) shaping and cassette tilting, as clarified later in section 3), it can be clearly seen that, from a relative displacement of 6 cm onwards, the strike point on the inboard side is already on the inner reflector plate (IRP), switching the target configuration from vertical to horizontal. On the low field side, see figure 4(b), the outboard strike point always remains on the vertical target, resulting in an almost constant total strike point angle.

The operational scenario for the nominal strike point position case, as well as for the displaced cases, corresponds to an ITER burning plasma scenario at  $Q_{DT} = 10$ , corresponding to  $q_{95} = 3$  operation at 15 MA and 5.3 T. This is the baseline Type I ELMing H-mode scenario, established by decades of tokamak R&D within the ITER partners and on the basis of which the ITER confinement time scaling was derived [19]. Deuterium (D) gas puffing at  $1.14 \times 10^{23} \text{ s}^{-1}$  (corresponding to pumping speed of  $\sim 38 \text{ m}^3 \text{ s}^{-1}$ , since puffing and pumping are balanced in these steady state simulations) gives a subdivertor neutral pressure of  $\sim 6$  Pa. Extrinsic seeding of Ne is added for detachment control. In the simulations, both fuel and impurity are introduced from a puffing slot at the top of the main chamber (see figure 2). This gas puffing location has been chosen consistently with that adopted so far in the ITER SOLPS database. Unpublished studies have demonstrated that the choice of gas introduction position has no

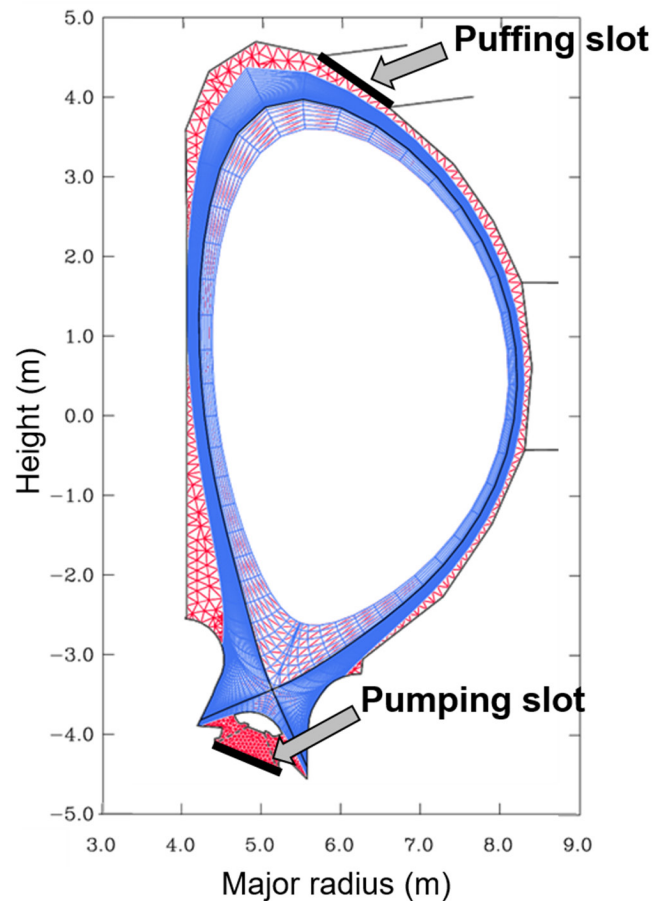


**Figure 2.** Computational grids for the B2.5 (in blue) and EIRENE (in red) codes adopted for the nominal strike point position case. The puffing slot at the top of the main chamber and the pumping slot below the dome have been identified with a thick black line.

impact on the results of steady state modelling, as performed here. Scrape-off layer transport timescales are short enough that the same steady state equilibrium is reached wherever the gas is puffed. The Ne puffing rate in the simulations is varied through a feedback loop which controls the total Ne content

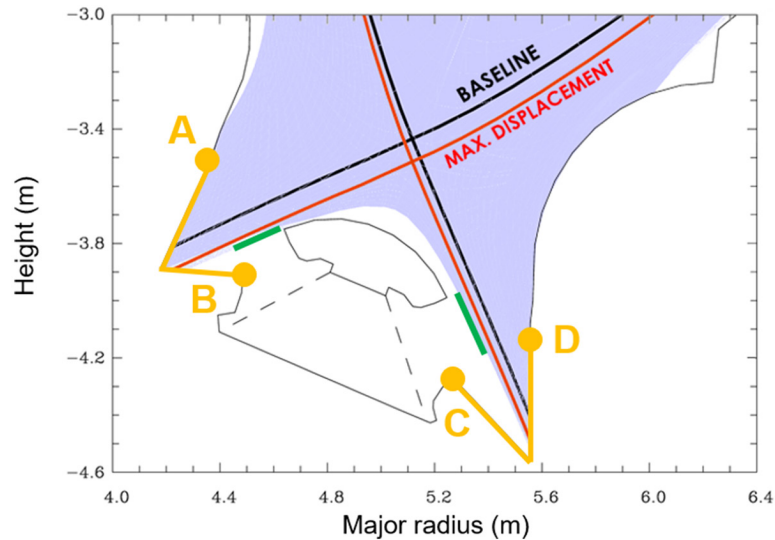


**Figure 3.** Plot of the separatrix for the baseline case with nominal strike point position (black) and for the maximum (8 cm) displacement case (red). The green lines at the boundary of the B2.5 grid show the regions over which the neutral pressure in the sub-divertor region is evaluated from the simulations. The yellow lines between points (A and B) and (C and D) identify the curvilinear plot domains on the divertor walls, see section 4.1.1.

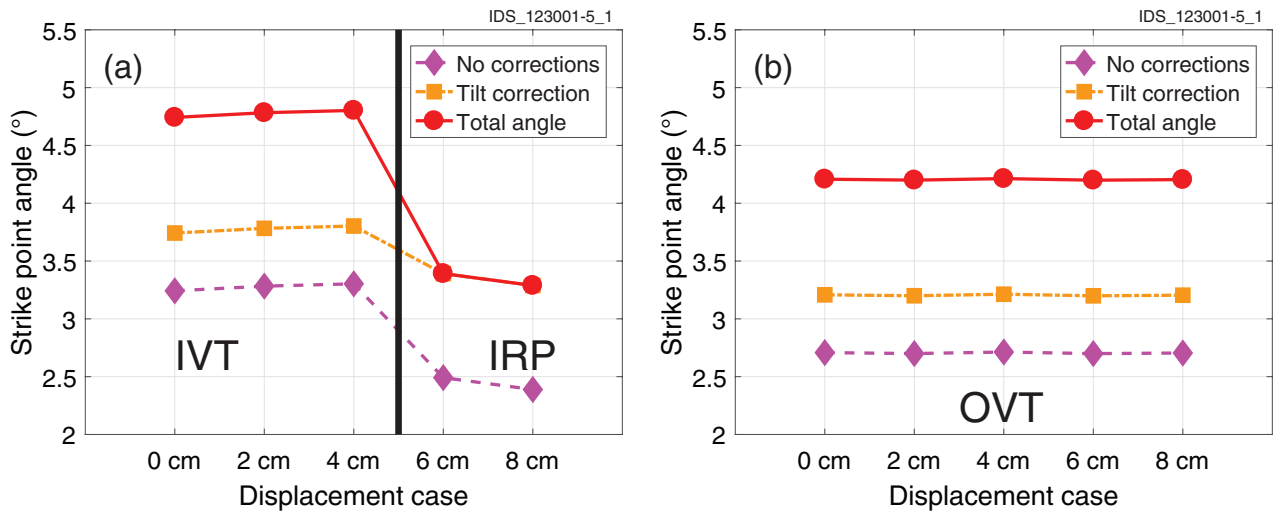


**Figure 4.** Strike point angles for the inboard (a) and outboard (b) divertor targets as a function of the equilibrium displacement. Purple dashed lines with diamonds do not take into account any component shaping or tilt correction; orange dash-dotted lines with squares account for the  $0.5^\circ$  VT tilting and the  $0.9^\circ$  IRP tilting; red solid lines with circles account also for the  $1^\circ$  monoblock top surface bevel. The vertical black thick line in (a) separates the cases at which the inner strike point is on the IVT from the point where it falls onto the IRP. The outer strike point remains on the OVT throughout.

within the SOL region. It therefore varies between the different runs performed and on average is  $2.4 \times 10^{20} \text{ s}^{-1}$ . This sets an upstream (outer midplane separatrix) Ne concentration relative to the electron density of  $\sim 1.8\%$ , which is on the high side of values considered consistent with core plasma performance (see [10]). The conclusions of this work will apply equally to scenarios with lower levels of Ne seeding.

The physical boundaries of the simulation domain have been modelled as follows: the VTs, RPs and dome are treated as W surfaces, with recycling coefficients set to 1 for all species and without erosion; for the first wall (FW) a Be surface has been adopted with 100% recycling and with Be physical sputtering taken into account [20]. Additionally, the dome supporting structure is treated as a semi-transparent stainless steel

(SS) surface (transmission coefficient 0.5). The pumping of neutral particles has been modelled assuming a fixed absorption coefficient for the SS surfaces in the region below the dome indicated in figure 2.

The plasma species considered in B2.5 are all the ionisation stages of D, He, Be (the latter originating from physical sputtering of the main chamber walls) and Ne, while the EIRENE model takes into account the neutral atoms of the above plasma species and in addition the neutral molecules  $\text{D}_2$  and molecular ions  $\text{D}_2^+$ . The collisional model of EIRENE for atoms and molecules is that of [21], taking into account full non-linear neutral–neutral interactions and ion–molecule collisions.

Anomalous transport in the cross-field direction has been assumed, with constant diffusion coefficients for particles

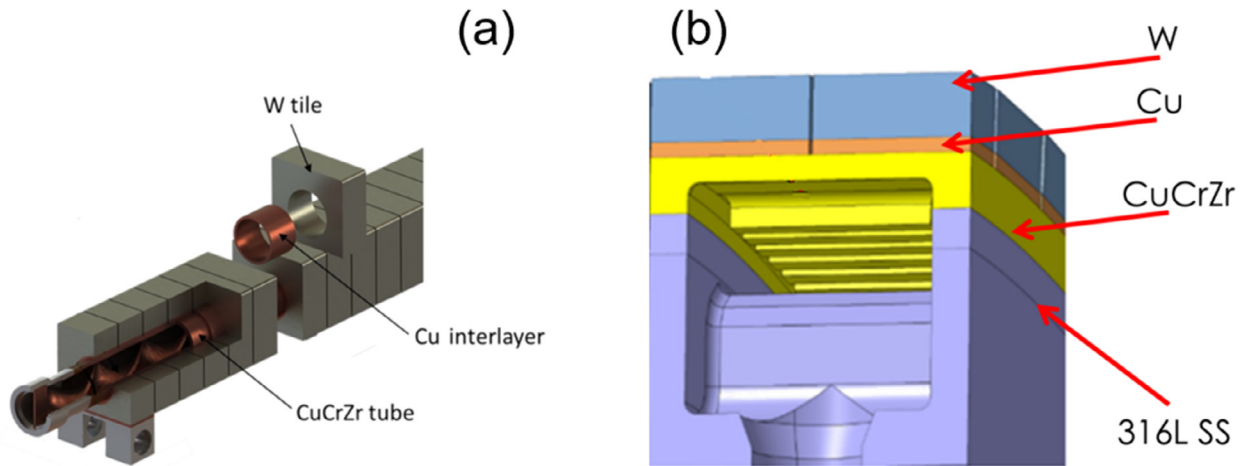


**Figure 5.** (a) Example of a monoblock of the ITER divertor (reprinted from [28], copyright 2017, with permission from Elsevier) and (b) cross-section of the RP or RP/dome plasma-facing unit.

$D_{\perp} = 0.15 \text{ m}^2 \text{ s}^{-1}$ , and heat  $\chi_{\perp} = 0.5 \text{ m}^2 \text{ s}^{-1}$ , and constant viscosity  $\eta_{\perp} = 0.2 \text{ m}^2 \text{ s}^{-1}$ . This choice of  $D_{\perp}$  and  $\chi_{\perp}$  yields a parallel heat flux density decay length  $\lambda_q \sim 2 \text{ mm}$  at the out-board midplane, a factor of 2 larger than the predicted value according to the most recent experimental scaling for 15 MA plasma current operation on ITER [22], but lower than the value of  $\sim 5.5 \text{ mm}$  recently obtained from fully turbulent simulations for ITER using the gyrokinetic code XGC1 [23]. Transport in the parallel direction is flux-limited and fluid drifts have not been activated in the simulations.

The distribution of the recycling neutrals from the surfaces is obtained through TRIM [24]. Divertor neutral pressure  $p_n$  is a key operational parameter for the machine (it determines He exhaust efficiency) and is defined here, as in previous work with SOLPS-4.3 [25], as the average over surfaces at the B2.5 boundary facing the openings towards the divertor subregion (see figure 3). It must be noted that since the B2.5 grid cells move with the displacements, the physical location of the surfaces for the pressure averaging is maintained as much as possible identical for all cases, although it does change slightly from case to case.

The main boundary conditions adopted in the plasma simulations are fixed decay lengths of 3 cm for density and temperature at the main wall and private flux region boundaries of the B2.5 computational domain, an imposed flux at the core boundary for particles ( $\Gamma_D^+ = 9.1 \times 10^{21} \text{ s}^{-1}$ ,  $\Gamma_{\text{He}}^{2+} = 2.13 \times 10^{20} \text{ s}^{-1}$ , corresponding to NBI and pellet core fuelling and fusion alpha production, respectively) and power ( $P_{\text{SOL}} = 100 \text{ MW}$ , equally split between ions and electrons). A standard Bohm boundary condition has been assumed at the targets. ADAS 96 reaction rates [26] have been used in the simulation for both fuel and impurities.

The B2.5-EIRENE simulations have reached steady-state, a condition identified by the particle and energy content characteristic timescales larger than 0.5 s and 3 s respectively [15]. Even though the particle confinement timescale is always larger than the energy confinement timescale, we have set these threshold values to obtain a trade-off between

the accuracy of the results and the CPU-time required by the simulations.

The SOLPS-ITER runs produced for this work have been assigned interface data structure (IDS) case identification numbers for storage within the ITER integrated modelling analysis suite (IMAS) [27] of 123001\_1, 123002\_1, 123003\_1, 123004\_1 and 123005\_1, corresponding respectively to the 0–2–4–6–8 cm displacements.

### 3. A heat transfer model for the ITER plasma facing components

To develop an ad hoc, simplified model to assess the thermal response of the ITER divertor PFC, the cooling technology adopted for the VTs and RPs has been examined and is briefly summarized below. An example of the VT W monoblocks is shown in figure 5(a): the CuCrZr tube is bonded to the W tiles through an interlayer of copper. A CuCrZr swirl tape inserted into the tube enhances the heat transfer between the coolant (subcooled water) and the solids.

The monoblocks constituting the VTs are not perfectly rectangular due to the shaping applied on the top surface. The baseline design consists of a toroidal bevel (figure 6) with bevel angle  $\beta \sim 1^\circ$  sufficient to protect, with some margin, a maximum allowed radial misalignment of 0.3 mm between toroidally adjacent monoblocks [8, 28]. Such leading edges, if not magnetically shadowed, would easily melt under transient heat fluxes induced by edge localized modes or disruptions [28, 29]. The price to pay for leading edge protection is an increased magnetic field line incidence angle and therefore increased heat flux density on the plasma wetted surface. Additionally, the entire vertical targets are tilted by an angle  $\alpha \sim 0.5^\circ$  to avoid leading edges on monoblocks on the sides of the gaps between neighbouring cassettes [28, 29]. In figure 4, the sum of these additional angles ( $1.5^\circ$ ) has been added to the magnetic field line incidence angle obtained from the magnetic equilibrium assuming a cylindrically symmetric surface.

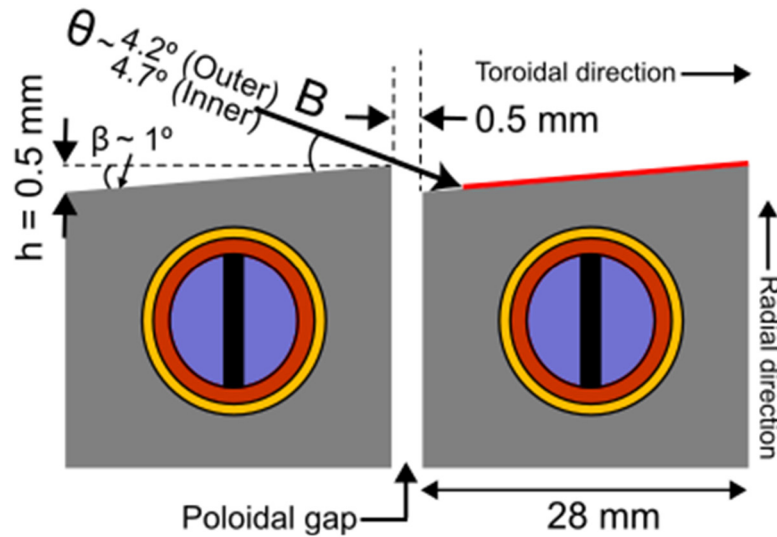


**Figure 6.** Cross-section of the divertor monoblocks with toroidal level. The values of  $\theta$  marked for the IVT and OVT are the total field line angles in the strike point region accounting for both the angle from the magnetic equilibrium and the monoblock level angle plus the global VT tilting. Reprinted from [28], Copyright 2017, with permission from Elsevier.

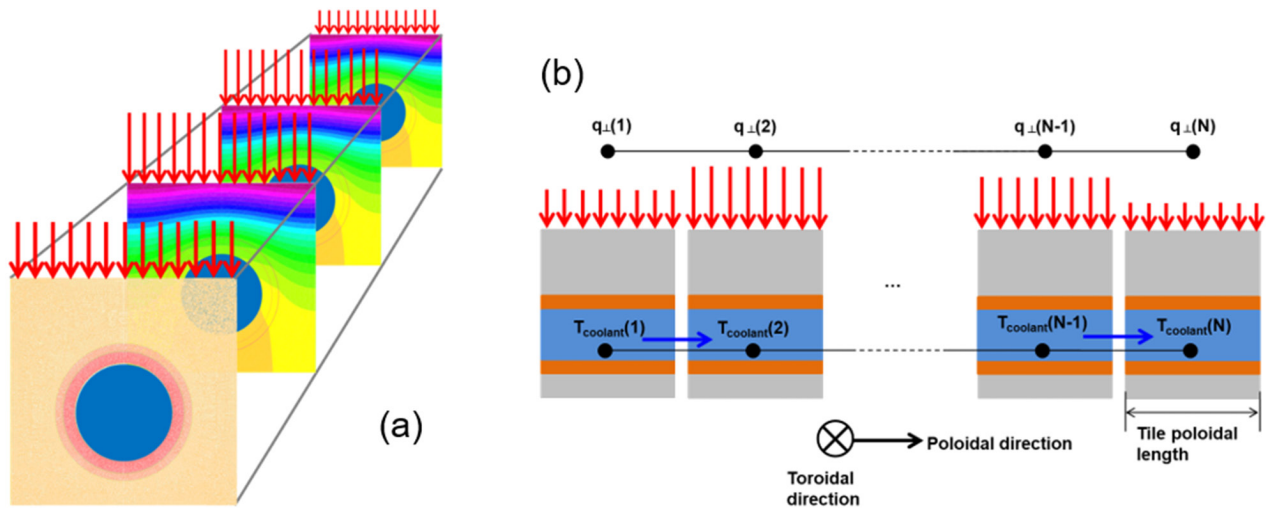


**Figure 7.** (a) Reduction of the 3D conduction and advection-diffusion problem of the monoblock thermal model into a series of 2D conduction problems on the monoblock cross-section, along the poloidal direction, coupled with an energy conservation equation for the coolant. (b) Schematic of the simplified heat transfer model of the monoblock along the coolant flow path (i.e. along the poloidal direction). The perpendicular heat flux  $q_{\perp}$  is represented by red arrows, the W solid in light grey, the Cu interlayer and CuCrZr tube in orange and the coolant in blue. The blue arrows indicate the direction of the fluid flow.

Regarding the RPs (and also the dome), they are made of W flat tiles (no top surface shaping), with hypervapotron cooling technology. Their configuration is shown in figure 5(b). The 316L SS support body is bonded to the corrugated CuCrZr hypervapotron surface. A Cu layer joins the W plasma-facing surface to the heat sink. Similar to the VTs, the RPs are also tilted toroidally (by  $\sim 0.5^{\circ}$  for the ORP and  $\sim 0.9^{\circ}$  for the IRP [30] to protect potential leading edges from cassette to cassette). This angle is taken into account in all calculations reported here of surface power density due to thermal plasma loads. It is also included in the total angle plots of figure 4.

The coolant flow path in the divertor is described in detail in [31]. Water is first fed in parallel to the monoblocks of the OVT from the V-shaped corner formed with the ORP. It

then flows poloidally to the top of the outer divertor baffle. Similarly, coolant enters the IVT and flows upwards to the top of the inner baffle. The outflow of the inner monoblocks is fed to the IRP hypervapotron channels, with the inlet near the corner with the VT and the outlet towards the dome, which is the next component in the loop, passing through the SS supporting tubes. Finally, the outlet of the dome is connected to the inlet of the outer RP having a flow direction from the dome towards the outer VT.

A simplified model of the PFCs has been developed here based on FreeFEM++ [32], an open-source software package for 2D/3D finite element computations. The package includes a mesh generator and allows the choice among a wide range of finite elements, integrated linear solvers and visualization tools. The simplified model developed has been made

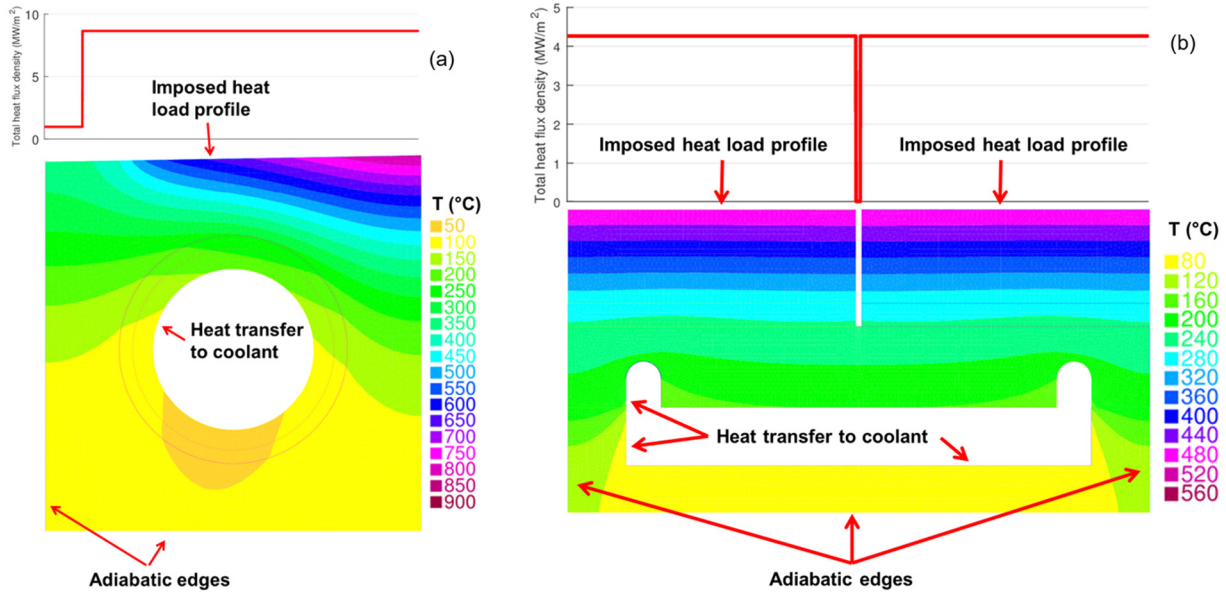


**Figure 8.** Example of 2D cross-sections with description of the applied boundary conditions for the simplified heat transfer model. (a) Monoblock with temperature distribution referring to the cross-section of the most loaded tile ( $\sim 8.7 \text{ MW m}^{-2}$ ) of the OVT for the case at 6 cm displacement, taking into account the shadowing due to the toroidal bevel. (b) The RP hypervapotron with temperature distribution referring to the cross-section of the most loaded tile ( $\sim 4.2 \text{ MW m}^{-2}$ ) of the IRP for the case at 8 cm displacement. The imposed heat load profiles on the top surfaces are shown for each case.

available within the SOLPS-ITER code package and allows the user flexibility to adapt the model to different cooling arrangements.

Beginning with the VT monoblocks, the first simplifying assumption made is to split the 3D problem into a series of 2D problems on the monoblock cross-section (figure 6), along the poloidal direction (see figure 7); on each section the heat diffusion in the solid is studied and the presence of the coolant is considered only as a boundary condition for the 2D conduction problem, i.e. no advection-diffusion computation is carried out on the fluid domain, as proposed in [33]. This assumption can be justified by the fact that the Péclet number in this context is very high and thus the heat conduction along the poloidal direction is negligible with respect to the coolant advection. Regarding the fluid, the simple, steady-state, pure advection energy conservation equation:

$$T_{\text{coolant}}(i) = T_{\text{coolant}}(i-1) + q_{\perp}(i) \cdot \frac{A_{\text{top}}(i)}{c_p \cdot \dot{m}} \quad (1)$$

is applied between adjacent 2D cross-sections along the poloidal direction, assuming a constant mass flow rate and specific heat capacity, see figure 7(b), where  $T_{\text{coolant}}$  is the coolant temperature,  $i$  is the discretized coordinate along the poloidal direction,  $q_{\perp}$  is the heat flux density normal to the surface,  $A_{\text{top}}$  is the area of the top surface subject to the heat load,  $c_p$  is the coolant specific heat and  $\dot{m}$  is the coolant mass flow rate.

It must be noted that the heat transfer along the poloidal direction in the CuCrZr tube and Cu interlayer has been neglected, meaning that the only coupling between one discretization node and the other is the fluid temperature. The discretization step between each 2D monoblock cross-section along the poloidal direction can be chosen small enough to

have both an acceptable accuracy in the solution and computational cost. In our case this is equal to the monoblock poloidal length (12 mm).

As far as the 2D conduction problem is concerned, see figure 8(a), the top surface of the monoblock experiences an imposed heat flux boundary condition, while the other outer edges are modelled conservatively with an adiabatic boundary condition, namely that there is no heat transfer between monoblocks along the toroidal direction nor with the supporting structures below. This condition, together with the adiabatic assumption between the tiles in the poloidal direction described above, implies that the model will provide an upper estimate of the temperature profile. On the inner side of the CuCrZr pipe, a Robin boundary condition is applied, with a constant coolant temperature and a convective heat transfer coefficient calculated according to the Sieder-Tate and Thom-CEA [34] correlations, corrected to account for the swirl tube effect, respectively for the forced convection and subcooled boiling regimes. When solving the conduction problem on each cross-section, temperature dependent material properties are taken into account, adopted from the ITER Materials Handbook, an internal document specifying which properties to use for all ITER machine materials when doing analysis studies.

In the poloidal direction (figure 7(b)), the surface heat flux density,  $q_{\perp}$ , is assumed to be constant on any given discrete poloidal element. Toroidally, the top surface bevel introduces magnetically shadowed and plasma wetted regions (figure 6). Photonic radiation and neutral particles will contribute to the heat load across the whole toroidal extent, but the charged particle loads occur only on the plasma wetted portion (red line in figure 6). These latter loads are dominant in anything but the most detached conditions. As mentioned earlier, the

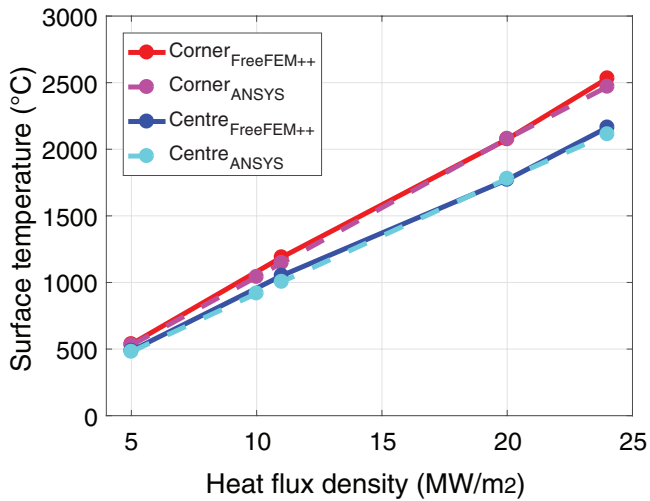


**Figure 9.** Results of the benchmark between the 2D FreeFEM++ model (solid lines) and the 3D ANSYS model (dashed lines) of a VT monoblock. The calculated temperature at the corner (red and purple) and at the centre (blue and cyan) of the top surface of the tile is plotted against the imposed heat flux density.

thermal plasma loads obtained from the SOLPS-ITER code must also be corrected for the VT tilt angle,  $\alpha$ , and the monoblock toroidal bevel angle,  $\beta$ , so that along the toroidal surface of each monoblock,  $q_{\perp}$  varies according to:

$$q_{\perp} = \begin{cases} q_{\text{neutr}} + q_{\text{rad}} & \text{for non wetted areas} \\ q_{\perp,\text{plasma}} + q_{\text{neutr}} + q_{\text{rad}} & \text{for wetted areas} \end{cases} \quad (2)$$

The FreeFEM++ 2D model of a monoblock tile has been benchmarked against results from ANSYS [35] 3D simulations of a monoblock performed within the ITER Organization. Figure 9 shows the results of the benchmark in terms of the temperature reached, in the corner and centre of the top (loaded) surface, as a function of the imposed heat flux density. Clearly, the FreeFEM++ model is in very good agreement with the 3D ANSYS counterpart.

The same simplifying approach adopted for the monoblock has been also applied for the hypervapotron channels of the RPs, see the cross-sections in figures 5(b) and 8(b). The indented structure of the CuCrZr has been reproduced in the FreeFEM++ model, see figure 8(b), where a Robin boundary condition has been applied with a heat transfer coefficient again calculated from the correlations in [34], adjusted for the hypervapotron configuration. The top surface, as in the case of the monoblocks, experiences the plasma/neutral/radiation heating and therefore the applied BC is an imposed heat flux. The outer edges are supposed to be adiabatic exactly as in the case of the monoblocks. Similar to the simplified monoblock model, the RPs have been discretized along the poloidal direction (which is also the coolant flow direction) as in figure 7(b).

## 4. Results and discussion

### 4.1. Plasma simulations

Before analysing the results in terms of divertor plasma and wall loading, we first show in figure 10 the profiles of

electron density and temperature at the inboard and outboard midplanes for the reference position and all the subsequent downward vertical strike point displacements. Evidently, with the exception of the 6 and 8 cm displacement cases, in which the density and temperatures profiles at the inner midplane are slightly modified a few cm into the SOL (figures 10(a) and (b)), the vertical movements do not significantly affect the upstream behaviour. As explained later in section 4.1.2, this perturbation is caused by the increased neutral density in the inner divertor region once the strike point accesses the IRP, which propagates towards the midplane, together with an increased local ionisation.

In figure 11 we show the outer target heat flux density computed by projecting the radial profile of the parallel heat flux density at the outer divertor entrance (X-point) onto the target and then mapping back to the outboard midplane in the manner described in [6, 36] and thus not accounting for dissipation in the divertor volume. Clearly, the downward displacements also leave this quantity almost unaffected. From these profiles we have estimated a power decay length  $\lambda_q \sim 2.5$  mm, about a factor of 2 higher than the value predicted for ITER by the most recent experimental scaling law, see section 2.

#### 4.1.1. Effects of the displacement on the divertor loading

Figure 12 summarizes the findings regarding heat loading on the inner and outer divertor target surfaces, where the total heat flux density (including thermal plasma, neutral particles and photons) is plotted as a function of the distance from the strike point along the divertor contour ( $s - s_{\text{sep}}$ ) defined in figure 3. The dash-dotted profiles in figure 12 (and in all forthcoming figures showing spatial profiles along the targets) denote cases in which the magnetic equilibrium displacement puts the inner strike point onto the IRP, thus switching from a vertical to a horizontal target configuration. All heat loads have been corrected to account for the  $0.5^\circ$  global component tilting (VTs and RPs) and the  $1^\circ$  top surface shaping of the monoblocks. Moreover, the plots have been restricted to 10 cm near the strike point since this is the region with largest heat flux density and where detachment can be observed. In these plots, the SOL region always corresponds to positive abscissa with negative values lying in the PFR. Collapsing the data in this way more clearly demonstrates the almost unchanged OVT heat loading with displacement, whilst illustrating the strong impact of the shift to the quasi-horizontal target when the strike point moves to the IRP (6–8 cm vertical plasma displacement). As explained below, this strongly modifies the detachment behaviour, reducing the thermal plasma contribution to the target load on the SOL side and enhancing the PFR loads due mainly to an increased contribution of radiation. It can also be observed that the total heat load at the strike point slightly increases (while the peak still decreases) in moving from the 6 cm to 8 cm downward displacement. As explained in section 4.1.2, this is due to a slight increase of the ion flux impinging on the surface when the strike point moves along the IRP away from the V-corner and the neutral density in the SOL region close to the separatrix decreases, reducing the load dissipation.

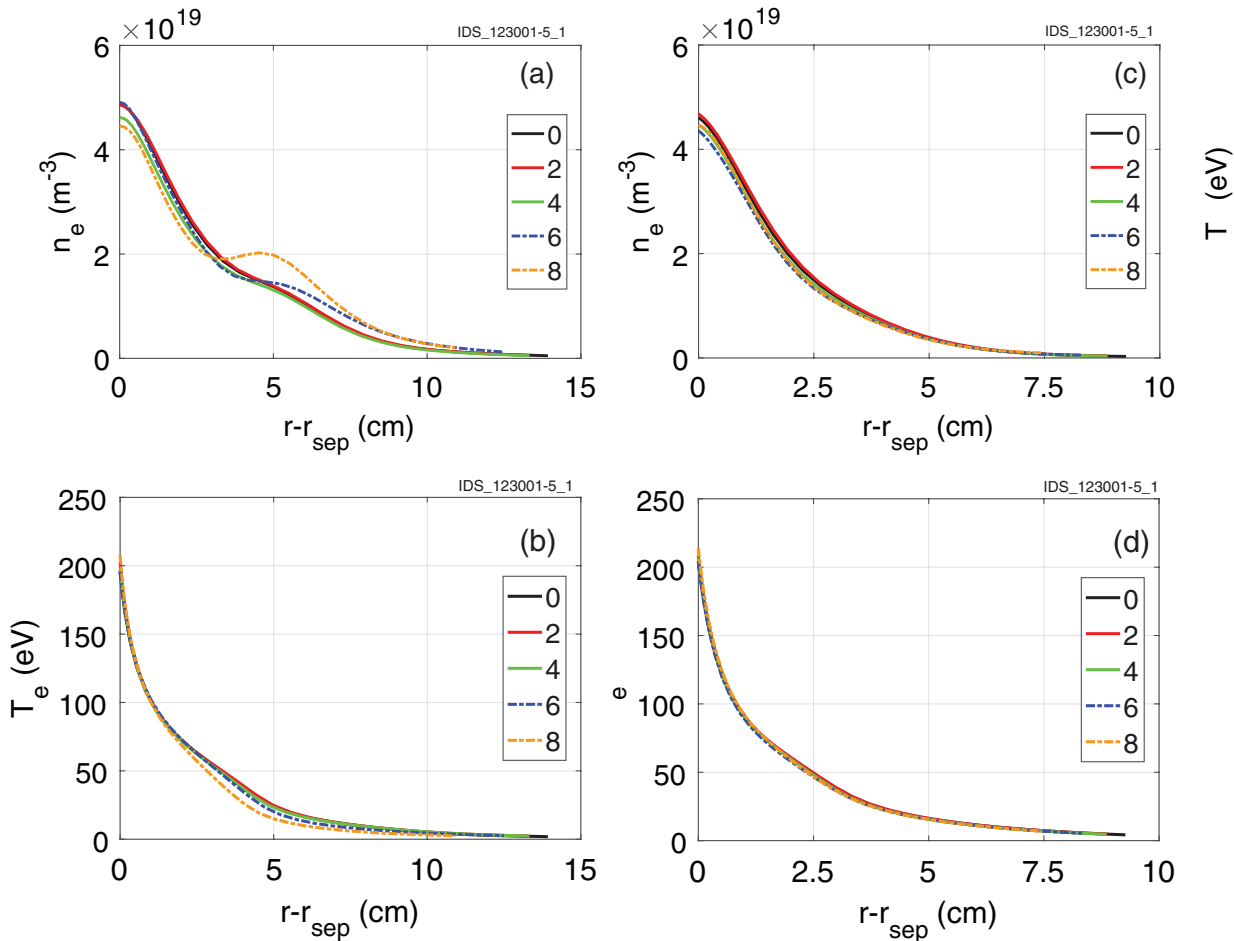


**Figure 10.** Plot of the midplane quantities as a function of the distance from separatrix for the different displacements: (a) electron density at the inboard midplane, (b) electron temperature at the inboard midplane, (c) electron density at the outboard midplane and (d) electron temperature at the outboard midplane. The solid lines correspond to the cases in which the inner strike point is on the VT while the dashed-dotted lines correspond to the cases in which the inner strike point lies on the IRP.

One may also note the high degree of symmetry in the peak power loading for configurations in which the strike points remain on the VTs. As specified earlier, fluid drifts are not activated in these simulations so any drift related asymmetries will be absent. However, very recent SOLPS-ITER runs for baseline conditions very similar to those employed here, but with drifts included, show that at the levels of sub-divertor pressure of the cases described here the in-out target loading is rather symmetric [37]. Even if drifts are ineffective, then a net out-in asymmetry is to be expected due to the toroidal geometry (higher surface area over which power can flow into the SOL on the low field side) and enhanced (ballooning like) outboard transport [38]. No radial transport asymmetry has been imposed in the simulations reported here and the geometrical power flow asymmetry is partially compensated (to the level of  $\sim 20\%$ ) by the divertor geometry, with the higher poloidal inclination at the IVT compared to the OVT steepening the total attack angle (see figure 4).

The histograms in figure 13 separate the three different contributions to the total heat flux density at the strike point (plasma, neutrals and photonic radiation). At the outboard

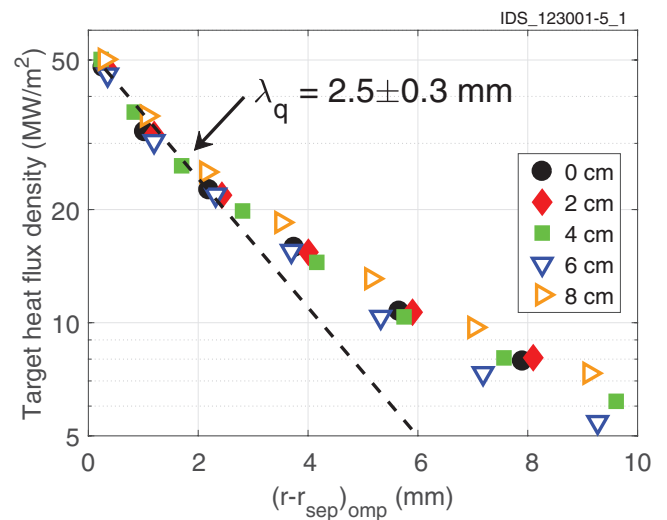


**Figure 11.** Outer target heat flux density mapped at the outboard midplane as a function of the distance from separatrix. The cases with a horizontal target configuration at the inboard side are identified with empty symbols. The black dashed line is the exponential fit of the points in the first 3 mm.

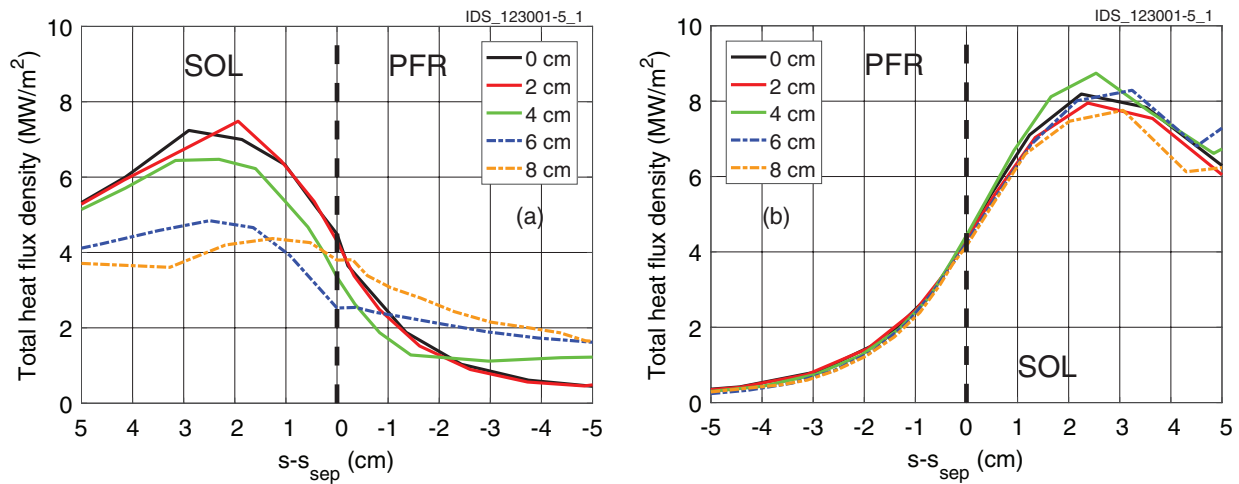


**Figure 12.** Total heat flux density on (a) the inboard and (b) the outboard divertor, as a function of the distance from the strike point along the divertor contour (see figure 3 and main text). Cases with strike points on the IRP are identified with a dash-dotted line.

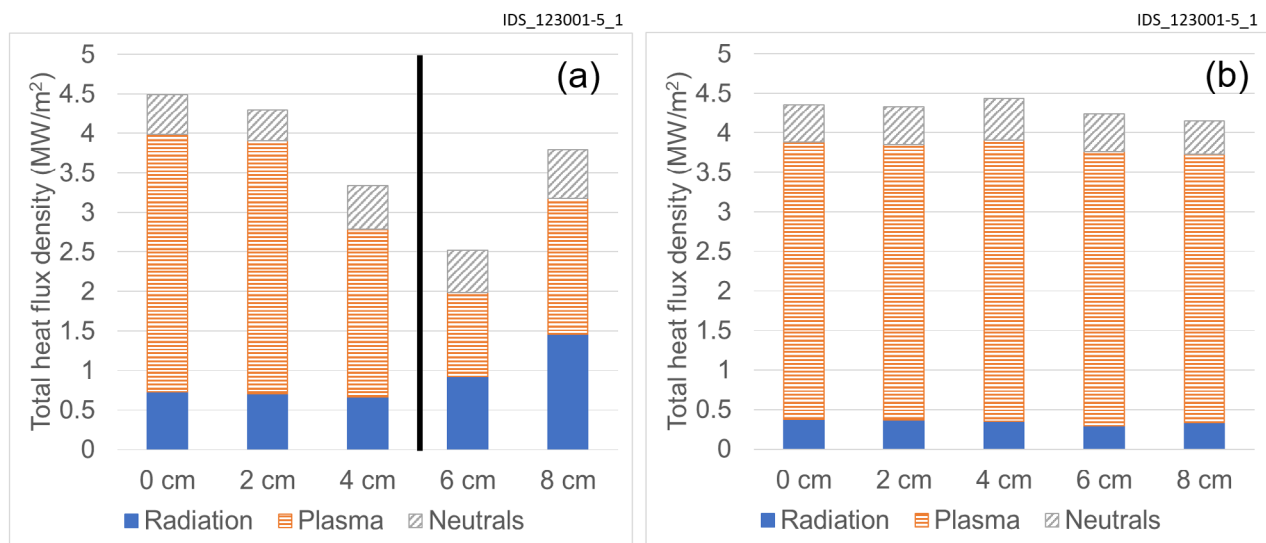


**Figure 13.** Split of the various contributions to the total heat flux density at the inner (a) and outer (b) strike points for the different displacements. The black vertical line in (a) separates the vertical target and horizontal target configurations.

divertor (figure 13(b)), consistent with the heat flux density profiles in figure 12(b), almost nothing changes as the plasma moves downwards, with the total heat flux density dominated by the plasma component. At the inboard (figure 13(a)), once the strike point moves onto the IRP, the photonic contribution increases to almost match the plasma load, for which  $\sim 30\%$  of the decrease can be attributed to the reduced attack angle (see figure 4), with the neutral component remaining relatively constant and close to its value for the vertical target configuration. This is a further sign of the change in detachment character. The slight increase of the plasma contribution when comparing the inboard values for the 6 and 8 cm displacement cases is attributed, as mentioned above, to a slight increase of the ion flux impinging onto the wall surface, see figure 16(a).

The plasma contribution can be further divided into two parts: the contribution from recombination of ions at the wall and the thermal contribution. Figure 14(a) compiles the

profiles of the recombination heat flux for the inboard divertor. Clearly, when the inner strike point remains on the VT the detachment degree is not significantly affected. However, when the displacement places the strike point onto the IRP, the total angle reduces (figure 4(a)) and simultaneously the switch to horizontal target configuration enhances the detachment. As mentioned above, the reduced angle accounts for  $\sim 30\%$  of the plasma heat load reduction at the strike point location (by the difference of the *sine* of the two angles divided by the *sine* of the larger angle since the parallel heat flux entering the inner divertor is essentially unchanged for the different displacements, see figure 15). The remainder must be attributed to the stronger detachment degree brought by the horizontal target geometry, which drives a total reduction of around a factor 2 of the recombination heat flux in the case of 8 cm displacement. This strong reduction (see figure 16(a) below), is due to a similarly strong reduction in the ion flux impinging onto the target surface. In contrast, on the OVT, the recombination heat

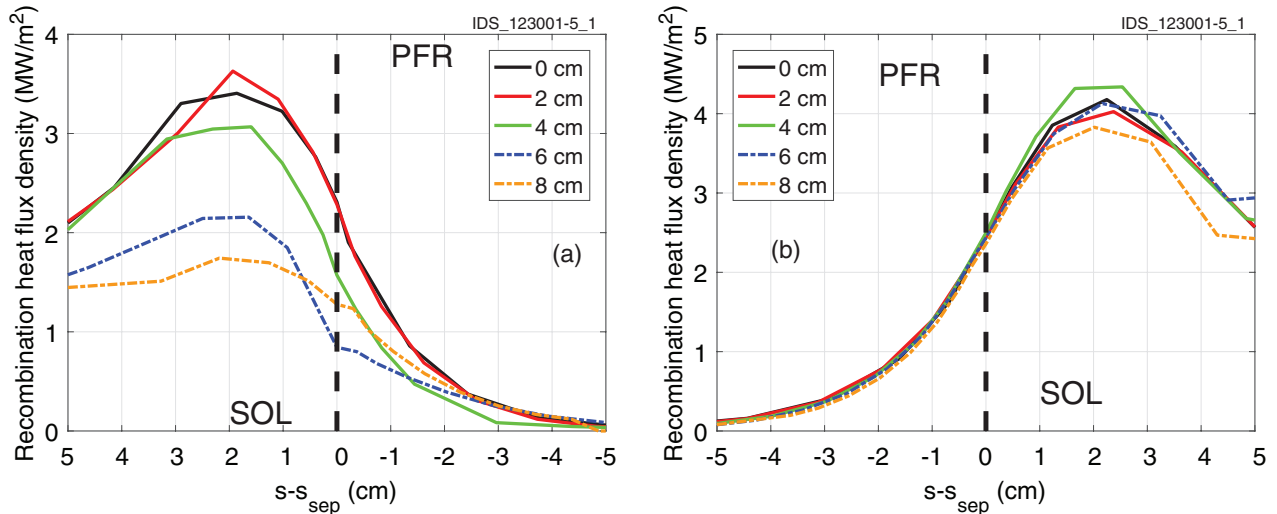


**Figure 14.** The recombination contribution to the total heat flux density on (a) the inboard and (b) the outboard targets, as a function of the distance from the strike point along the divertor contour.

flux density profiles remain largely unchanged with increasing vertical displacement, consistent with the unchanged detachment character.

Figure 16(a) shows how the flux of ions to the target in the maximum displacement case is reduced by a factor  $\sim 2$  with respect to the reference VT configuration. As will be demonstrated in section 4.1.2, this is due to the change in the neutral atom and molecule distribution within the inboard divertor region, leading to an increase in the momentum losses, as noted also in [39]. For the 6 cm case, a region of very high neutral density forms at the corner, close to the separatrix, see figure 24 in section 4.1.2, inducing a stronger detachment than for the largest displacement case. The outboard divertor profiles (figure 16(b)) remain largely superposed, with the exception of the 8 cm displacement, for which there is a small, but noticeable reduction in the peak ion flux density.

Examination of the second component of the plasma contribution, the thermal one, see figure 17, reveals a similar trend with respect to displacements to that observed for the recombination contribution (figure 14). The change from vertical to horizontal target configuration on the inboard side leads to a reduction of this contribution up to a factor 2, while the outboard side is almost unaffected. This contribution is driven by the plasma temperature and ion flux density. Since the plasma temperature at the plates barely changes on both the inner and outer divertor for all displacements (see figure 18) the main driver of the reduction in thermal contribution is the reduction in ion flux density seen in figure 16 for the inboard divertor. Similarly to the ion flux density profiles in figure 16, a slight difference between the 6 cm and 8 cm displacement cases is also seen in the inboard divertor electron temperature profiles. As a result of the increased neutral particle density, the momentum losses close to the separatrix are slightly larger for the case at 6 cm displacement, leading to a larger plasma power dissipation and, consequently, a lower plasma temperature. As mentioned above, this is also the origin of the reduced ion flux density to plate as the strike point access the IRP.

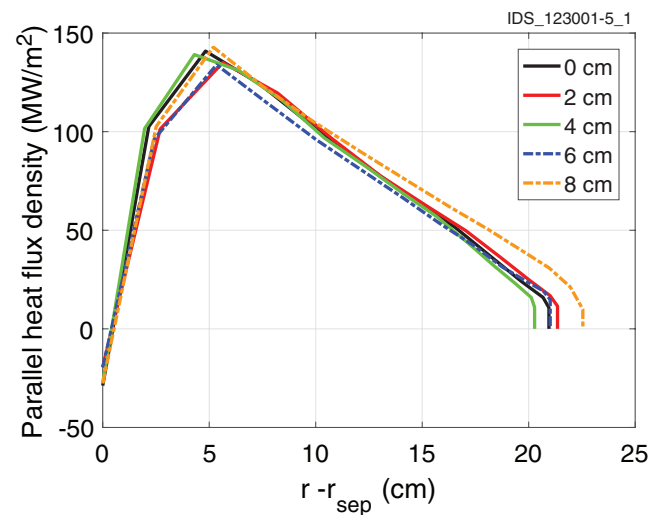


**Figure 15.** Radial profile of the total parallel heat flux density entering the inner divertor taken at the X-point point height and plotted as a function of the distance from the X-point.

The second contribution to the total heat flux is the radiation component, due to line and Bremsstrahlung radiation (both of which are included in the SOLPS-ITER modelling) from all the ionised atoms within the plasma, together with neutral excitation radiation. There is an additional contribution from core plasma radiation, due to cyclotron, synchrotron, Bremsstrahlung and line radiation, which is not modelled in SOLPS-ITER. This has been taken into account here approximately using a series of several sources uniformly distributed within the core for a total of 45 MW, consistent with the assumed core power losses for the original SOLPS-4.3 simulations used to establish the divertor operating range for  $P_{\text{SOL}} = 100$  MW. The plasma is assumed optically thin.

About  $\sim 88\%$  of the total radiation source is found within the divertor region (not including the imposed 45 MW core radiation), with a large contribution from Ne radiation ( $\sim 68\%$  of the total divertor radiation) and the remainder from D

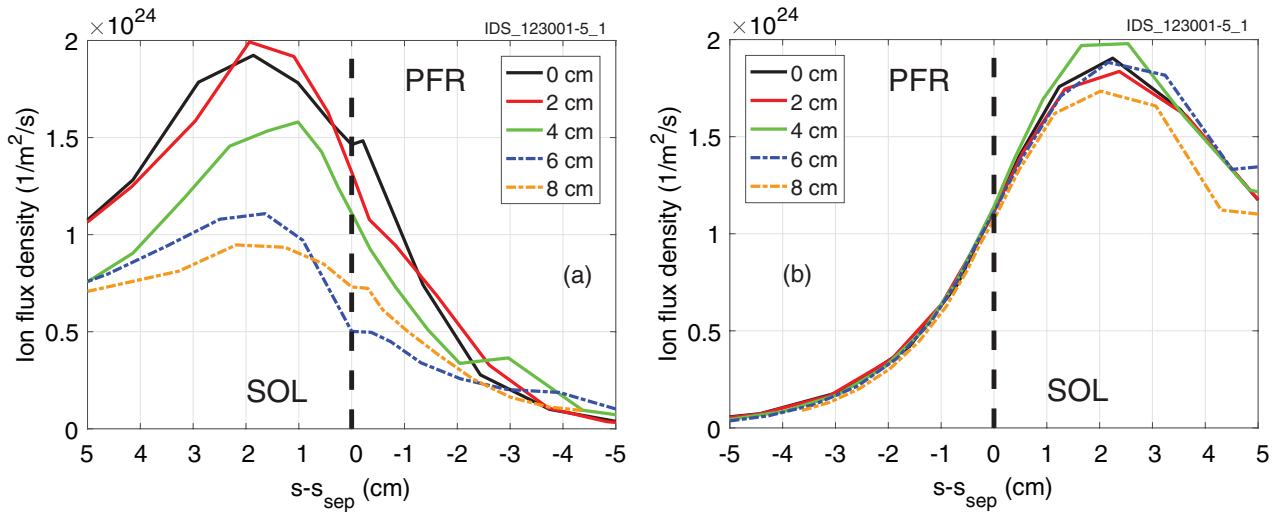


**Figure 16.** Ion flux density profiles on (a) the inboard and (b) the outboard divertor, as a function of the distance from the strike point along the wall.

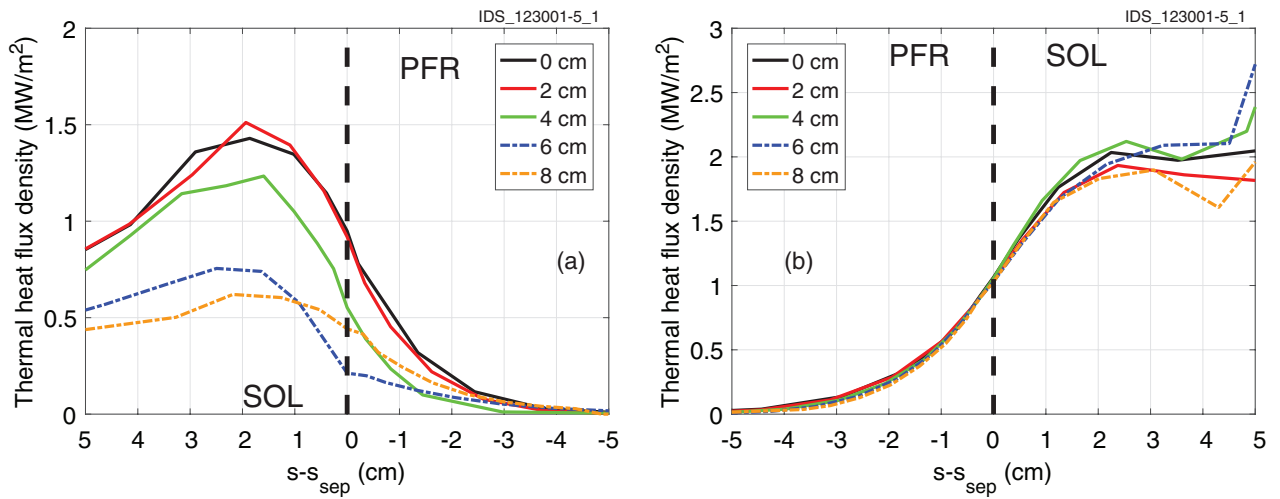


**Figure 17.** Plasma thermal contribution to the total heat flux density on (a) the inboard and (b) the outboard divertor, as a function of the distance from the strike point along the wall.

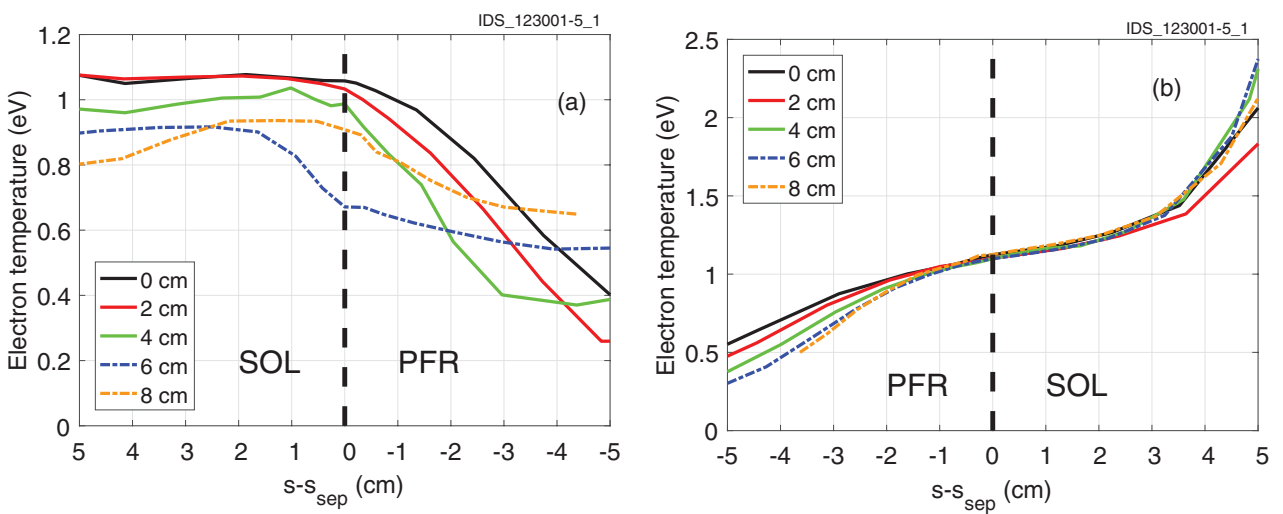


**Figure 18.** Electron temperature profiles on (a) the inboard and (b) the outboard divertor, as a function of the distance from the strike point along the wall.

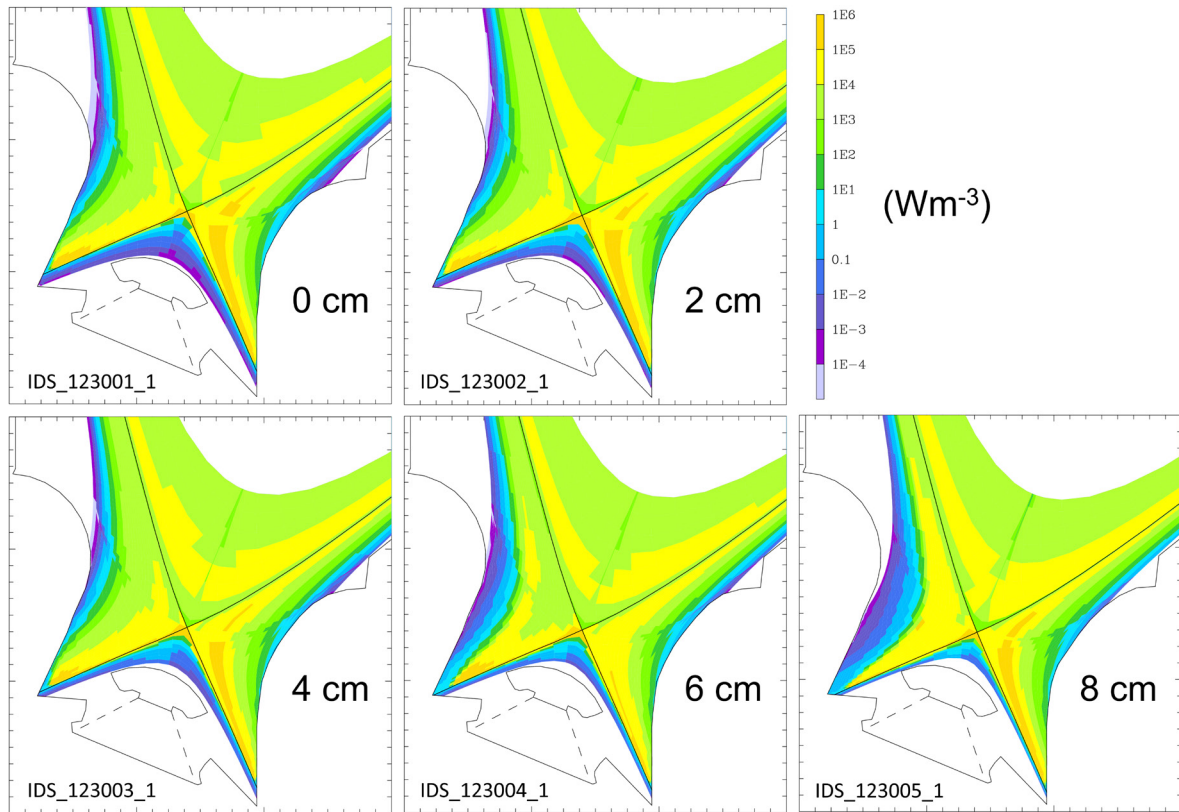


Figure 19. Distribution of Ne radiation source density in the divertor region for the different displacements.

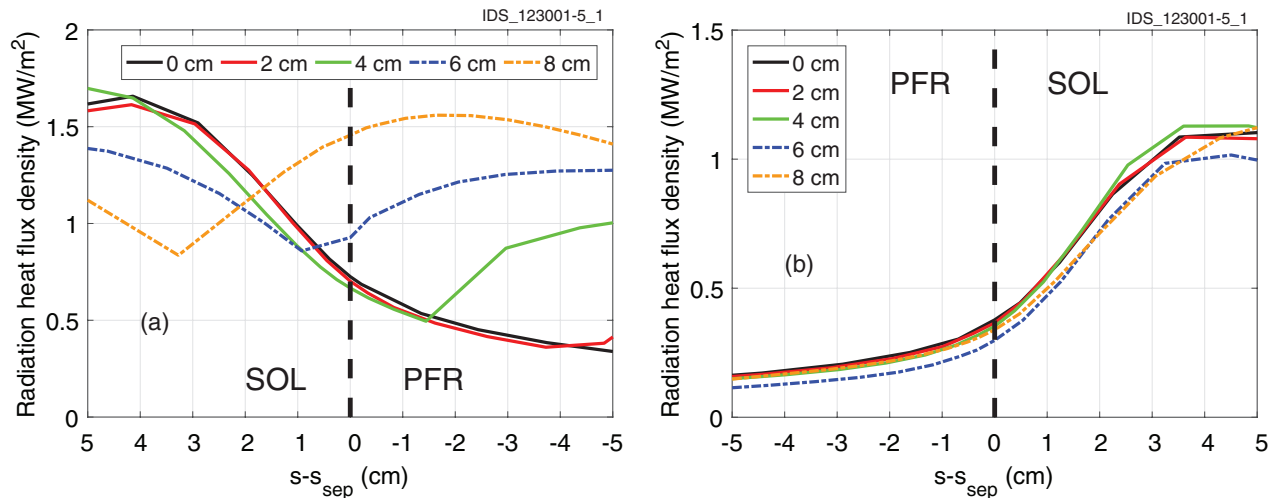
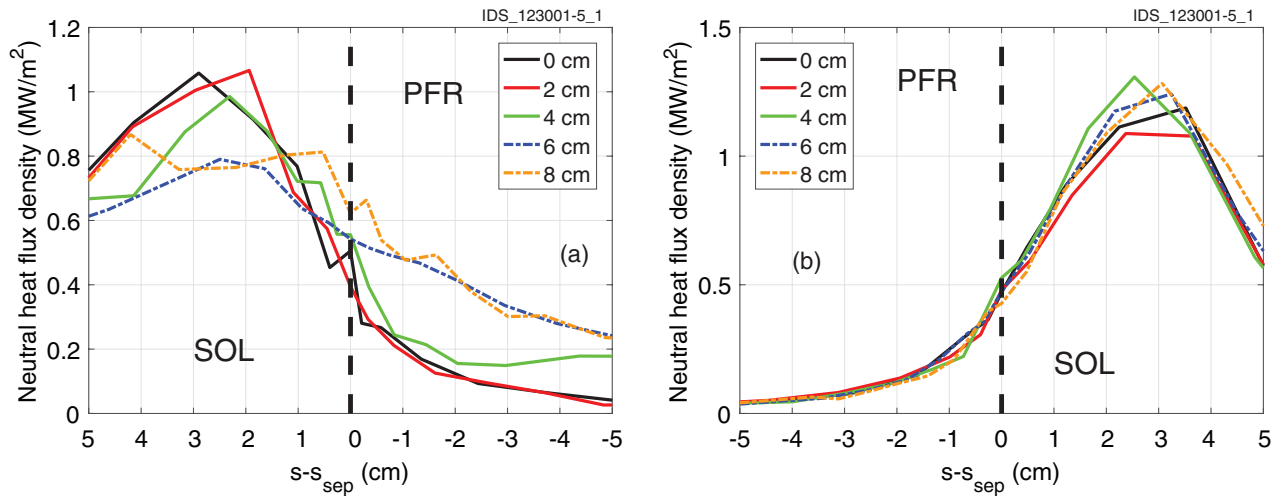


Figure 20. Radiation heat flux densities on (a) the inboard and (b) the outboard divertor, as a function of the distance from the strike point along the wall.

neutral excitation. Figure 19 illustrates the distribution of the Ne radiation source density in the divertor region for the different displacements, clearly indicating that the Ne radiation is well confined in the divertor region. The profiles of radiative heat flux density are given in figure 20(a) for the inboard divertor, showing discontinuities at the minima for the 4, 6 and 8 cm displacements due to the V-shaped geometry of the IVT–IRP intersection: the different inclination between IVT and IRP causes a difference in the view factor. This minimum moves to the left of the figure with increasing downward

displacement (the minimum for the 0–2 cm cases is located at an abscissa outside the range of the plot).

When switching to a horizontal target configuration, the total power radiated by the plasma increases slightly (+3% for the 6 cm case and +10% for the 8 cm case) due to a modified distribution of recycling leading to a higher ionisation of D atoms in the near SOL. This is discussed further in section 4.1.2 and has also been noted in [39]. In addition, the plasma itself has been displaced, bringing the radiation sources closer to the RPs. As a consequence, the radiation



**Figure 21.** Neutral heat flux densities on (a) the inboard and (b) the outboard divertor, as a function of the distance from the strike point along the wall.

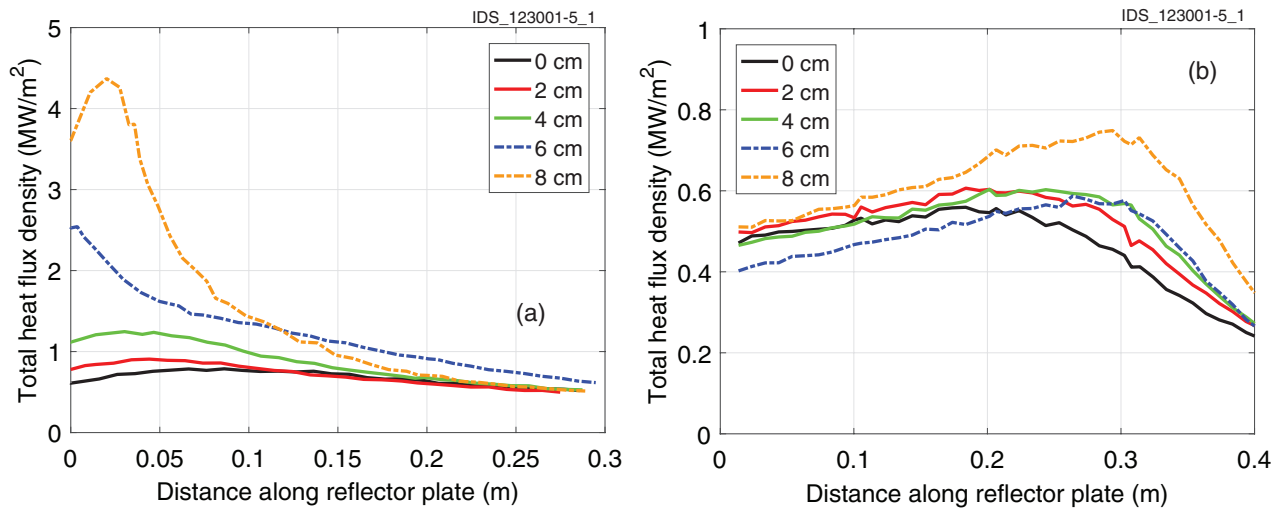


**Figure 22.** Total heat flux density on (a) the inboard and (b) the outboard RPs, as a function of the distance along the wall from the left edge of each RP.

contribution near the strike point and especially in the PFR increases, leading, as anticipated, to the broadening of the total heat load profile seen in figure 12(a). As usual, at the OVT, the radiative heat loads (figure 20(b)) are unaffected by the displacements, reflecting the unchanged detachment character as the plasma moves downwards.

The final contribution to the total heat flux density originates from neutral particles: atoms and molecules ( $D_2$ ); figure 21(a) compiles the profiles of this contribution along the walls of the inboard divertor. Once the inner strike point falls on the IRP, there is a significant ( $>$ factor 2) increase in the PFR neutral heat flux density as well as a slight increase at the separatrix. As expected (figure 21(b)) there is no change at the OVT, where the strike point remains on the vertical target for all plasma displacements.

The principal aim of this work is to provide general guidance for engineering heat loads to be expected on the divertor RPs and in particular to assess the likely increase in the magnitude of these loads in the case of plasma vertical displacements. We thus now focus for a moment only on the total RP

heat loads, beginning with figure 22, which compiles the total heat flux density profiles on the IRP and ORP, on this occasion plotted against distance from the left edge of the RP in each case. For the IRP, the origin is at the V-corner with the IVT whilst for the ORP, it is at the left edge below the outer dome wing. Figure 23 provides histograms of the different components to the total heat load, in analogy with figure 13.

In the case of the IRP (figure 22(a)), when the strike point is still on the VT, the main contribution is radiative (see figure 23(a)) and increases slightly as the plasma is moved down and closer to the plate (this is to be expected from purely geometrical considerations). Once the strike point hits the plate, switching to the horizontal target configuration, the thermal plasma makes contact with the plate surface, strongly increasing the total heat load. The maximum value,  $\sim 4 \text{ MW m}^{-2}$  in this case, is within 20% of the tolerable steady state heat flux density for the RP flat tile technology [40]. At the ORP, since the strike point remains on the OVT, the main contribution to the total load is radiative (see also figure 23(b)), increasing only slightly with increasing displacement (again

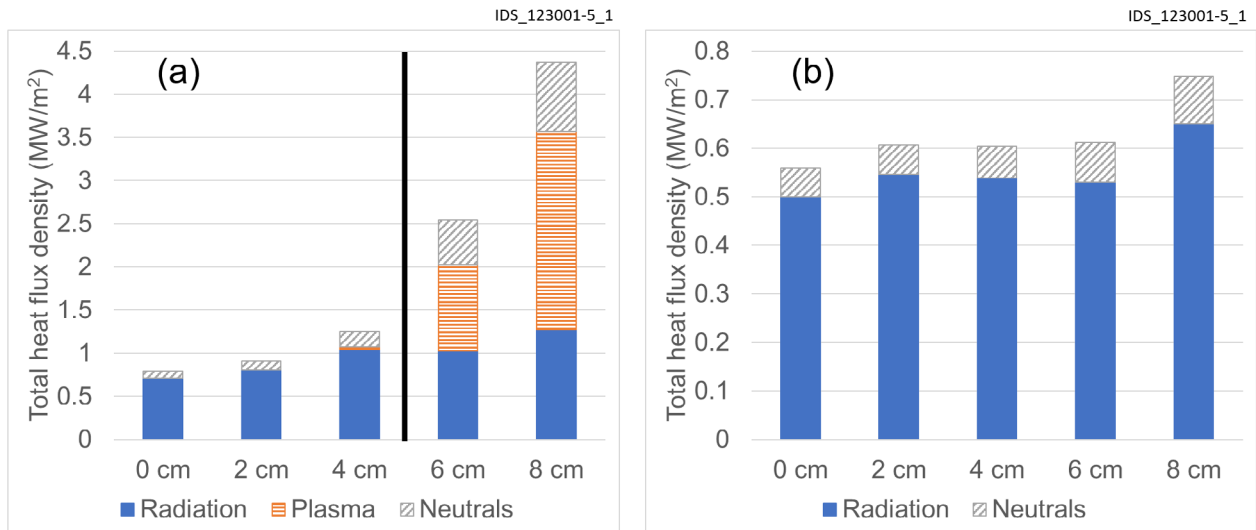


**Figure 23.** Histograms of the different contributions to the maximum heat flux density for the different displacements in case of (a) the inboard and (b) the outboard RPs. The black vertical line in (a) separates the cases with vertical target configuration from the cases with horizontal target configuration on the inboard side.

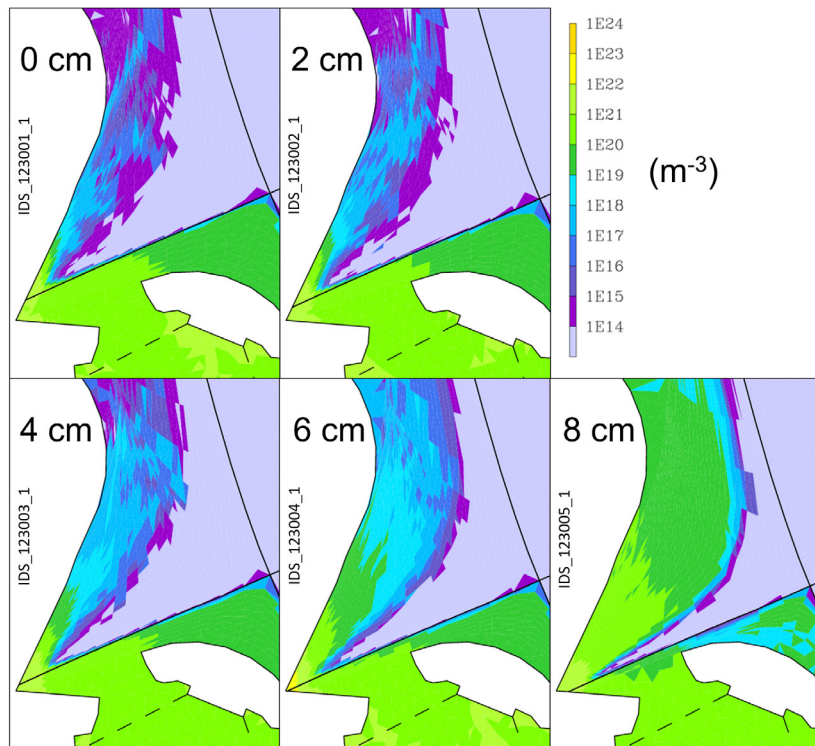


**Figure 24.** Distribution of neutral particle density (atoms + D<sub>2</sub> molecules) at the inboard divertor for the different displacements.

due to geometrical effects). The values are far below the maximum tolerable stationary heat loads.

**4.1.2. Effects of the displacement on neutral transport.** A clearer picture of the differences in the detachment characteristics when the target configuration on the inboard side is switched from vertical to horizontal can be obtained by analysing the distributions of neutral and plasma particle source density. The former is shown in figure 24 for the different displacements and accounts for both D atoms and D<sub>2</sub> molecules, which play a non-negligible role in the divertor region, where

the temperatures are low enough for molecule formation. In the vertical target configuration (0–2–4 cm displacements), the incoming ions are recycled as neutrals towards the separatrix and the PFR, building a cushion of dense neutrals in a small near SOL region typical of partially detached conditions. For the horizontal target configurations (6–8 cm displacements), the distribution is strongly modified, with an enlarged region of dense neutrals forming in the SOL plasma in front of the target and expanding towards the main chamber, leading to reduced plasma plugging. This region of high neutral density increases in size with the displacements and leads, for the 6

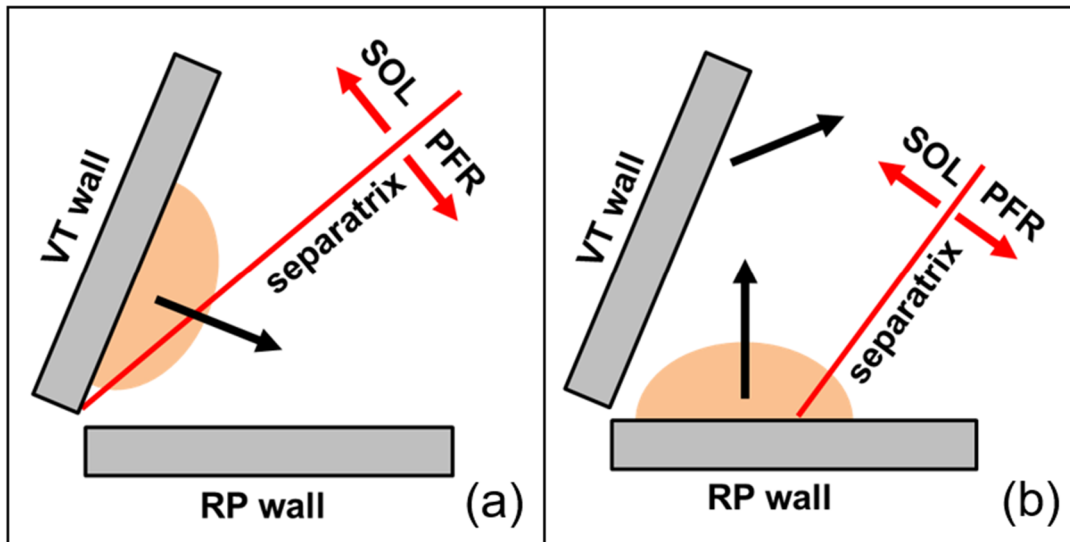


**Figure 25.** Schematic illustrating the different recycling distributions expected for (a) vertical and (b) horizontal target configurations.

and 8 cm displacements, to the mid-SOL perturbation seen in the inner midplane electron density profile of figure 10(a). This perturbation is caused by the neutral particles escaping from the inboard divertor region towards the main chamber. In fact, the neutral particle density at the inboard midplane, displayed in figure 26(a), shows a small increase for the 6 cm and a large increase for the 8 cm displacement cases. This is reflected in a significantly higher volumetric ionisation rate, shown in figure 26(b), localized around 5 cm from the separatrix, where the density perturbation is located (see figure 10(a)). Although the neutral particle density increases further towards the walls, the ionisation rate decreases so that the plasma density profile returns to values similar to the other displacement cases.

The increased neutral density in front of the plate increases the plasma momentum dissipation, therefore reducing the impinging ion flux, as shown in figure 16(a), and thus reducing the heat flux due to plasma particles. The reason for this dramatic change in the detachment behaviour is due to the different recycling of neutrals (see the schematic in figure 25), which, as also described in [14, 39], are now directed towards the SOL region and not the separatrix. In addition, the horizontal target inclination is such as to launch the neutrals against the VT, promoting recycling near the divertor region, especially when the strike point is close to the V-corner (6 cm displacement). For this displacement case, a region of high neutral particle density is formed very close to the separatrix (see the small yellow zone in figure 24), due to the strike point location right at the junction between the IVT and IRP (in fact just marginally on the IRP). Here, the neutral particles are recycled towards the (close) VT which re-emits them towards the separatrix, thus concentrating the neutral particles in this small region and enhancing the momentum losses, inducing a stronger detachment than for the largest displacement case, as described in section 4.1.1. As the plasma is further displaced downward in the 8 cm case, the distance between the strike point and the V-corner (and thus the VT) increases. This in turn increases the probability of neutral particle escape so that the high neutral particle density region is reduced in extent and

the momentum losses decrease. At this point, the main reservoir of neutral particles is not only the PFR region but also the SOL region, with implications also for the divertor neutral pressure and therefore pumping efficiency. The divertor neutral pressure (see figure 3 for the reference locations where this quantity is evaluated for the simulations) does not change monotonically as the plasma is displaced downwards and has a different trend for the inboard and outboard divertors, as reported in table 1. At the inboard, the average pressure remains almost constant for the 0–2–4–6 cm displacements and reduces down to  $\sim 84\%$  of its original value for the largest displacement, due to the different neutral recycling described above. On the outboard, it reduces by only  $\sim 5\%$  for the cases at 2 and 4 cm displacement and increases slightly above its original value for the case at 6 cm displacement to finally drop by  $\sim 17\%$ , for the largest displacement case, possibly due to the effect of the lower pressure at the inboard side or to the higher electron temperature close to the measurement area as the plasma is displaced downwards. In fact, as shown later in figure 28, the neutral density just outside the outer PFR decreases for the case at 8 cm displacement. The slight differences in the pressure values between the cases at 0–2–4–6 cm displacement can be attributed to the slightly different averaging surfaces for the pressure evaluation.

The pumping rate is directly affected by the PFR pressure and is sensitive to the overall decrease of the divertor pressure, as seen in table 1 for the largest vertical displacement when its value decreases by more than 50% compared with the reference position. On the other hand, the pumping rate at 6 cm increases by  $\sim 10\%$  with respect to the baseline case, as consequence of the slight increase of the overall divertor pressure.

Previous studies [4] have shown how a reduction in the average pressure in the PFR could affect plasma operation, through a reduction in the He ash removal (increased He density at the separatrix when the pressure reduces). Given that the average PFR pressure encountered in the cases at hand (table 1) does not change significantly, the He density at the midplane (table 2) is not strongly affected, so that He removal

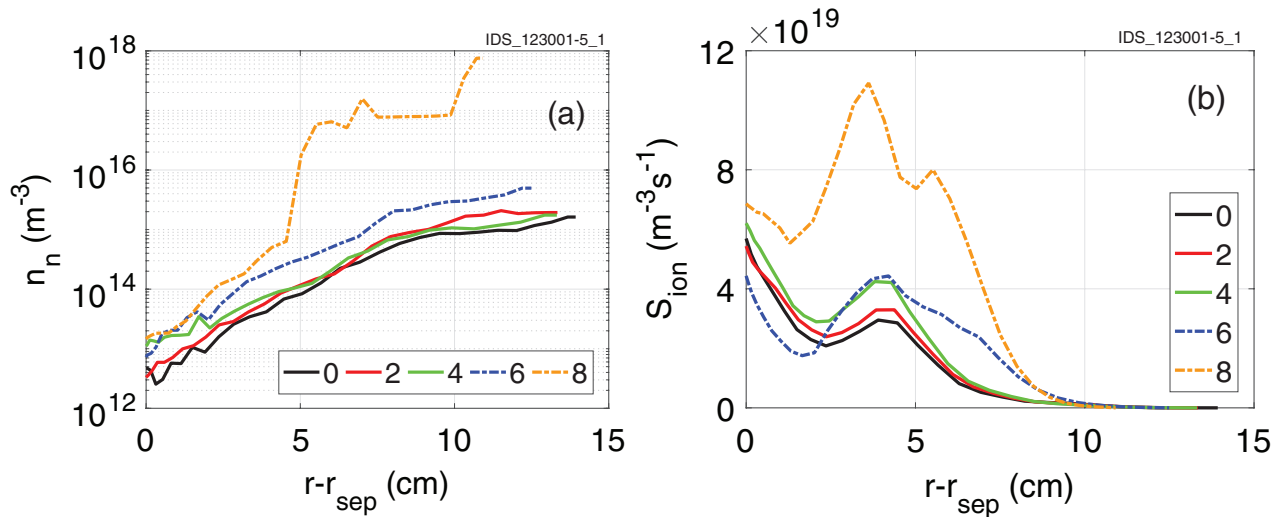


**Figure 26.** Plot of (a) the neutral particle density  $n_n$  (atoms +  $D_2$  molecules) and (b) the volumetric ionisation rate  $S_{ion}$  at the inboard midplane as a function of the distance from the separatrix for the different displacements.

**Table 1.** Divertor neutral pressure and neutral pumping rate (normalised with respect to baseline).

Case (cm)	Inboard divertor pressure (Pa)	Outboard divertor pressure (Pa)	Overall divertor pressure (Pa)	Normalised pumping
0	5.1	7.0	6.1	1.00
2	5.2	6.6	6.0	0.84
4	5.1	6.6	5.9	0.87
6	5.2	7.1	6.3	1.1
8	4.3	5.8	5.2	0.47

should not be compromised. The trend however, is not trivially linked to the divertor neutral pressure since, despite an overall decrease of the inboard divertor pressure with vertical displacement, the He density also decreases. It is worth noting, however, that configurations with inner strike point on the IRP will never be considered as stationary operating scenarios so that the question of any compromise in He exhaust efficiency is rather irrelevant.

Analysis of the 2D plasma particle source density distribution (figure 27) provides further insight into the differing detachment nature when the inner strike point falls on the IRP. A negative source, identified by the blue shaded regions in the plots of figure 27, indicates a relatively cold plasma region where recombination is predominant. A positive source, identified by the red shaded regions, is typical of an ionising plasma. In a standard semi-detached regime, as in the case of the vertical target configuration, an ionisation region is present in front of the target, with a small recombining region close to the strike point, where volumetric losses help to dissipate the incoming plasma power. When switching to the horizontal target configuration, the ionisation front is pushed away from the target, significantly expanding the recombination zone.

Regarding the OVT, the neutral particle density and source density distributions, shown in figures 28 and 29 respectively, remain essentially unchanged with increasing vertical displacement. They are typical of the vertical target partially detached solutions found for ITER (and indeed seen also at

**Table 2.** Separatrix He density at inboard and outboard midplanes.

Case (cm)	IMP ( $m^{-3}$ )	OMP ( $m^{-3}$ )
0	$3.0 \times 10^{17}$	$3.0 \times 10^{17}$
2	$2.8 \times 10^{17}$	$3.0 \times 10^{17}$
4	$2.6 \times 10^{17}$	$2.7 \times 10^{17}$
6	$2.8 \times 10^{17}$	$2.7 \times 10^{17}$
8	$2.1 \times 10^{17}$	$3.0 \times 10^{17}$

the IVT for strike points away from the IVT-IRP corner), with the ionisation front tight to the plate and a strongly recombining region only very close to the strike point. This can be seen as an indication of the strong neutral-neutral interactions on ITER, as discussed in [2], which dominate over any modifications which might occur due to target geometry as the strike point descends deeper into the outer divertor slot. To see this, an estimate of the neutral mean free path  $\lambda_{mfp}$  can be made according to the following equation, similar to equation (4) in [41]:

$$\lambda_{mfp} = \frac{v_n}{f_{CX} + f_{ion} + f_{n-n}} \quad (3)$$

which gives  $\lambda_{mfp} \sim 1$  mm for the inboard divertor, much smaller than the divertor dimension. In equation (3)  $v_n$  is the neutral average velocity,  $n_e$  is the electron density,  $f$  is the frequency of charge-exchange ‘CX’ collisions, ionisation ‘ion’ collisions and neutral-neutral ‘n-n’ collisions. The estimated average

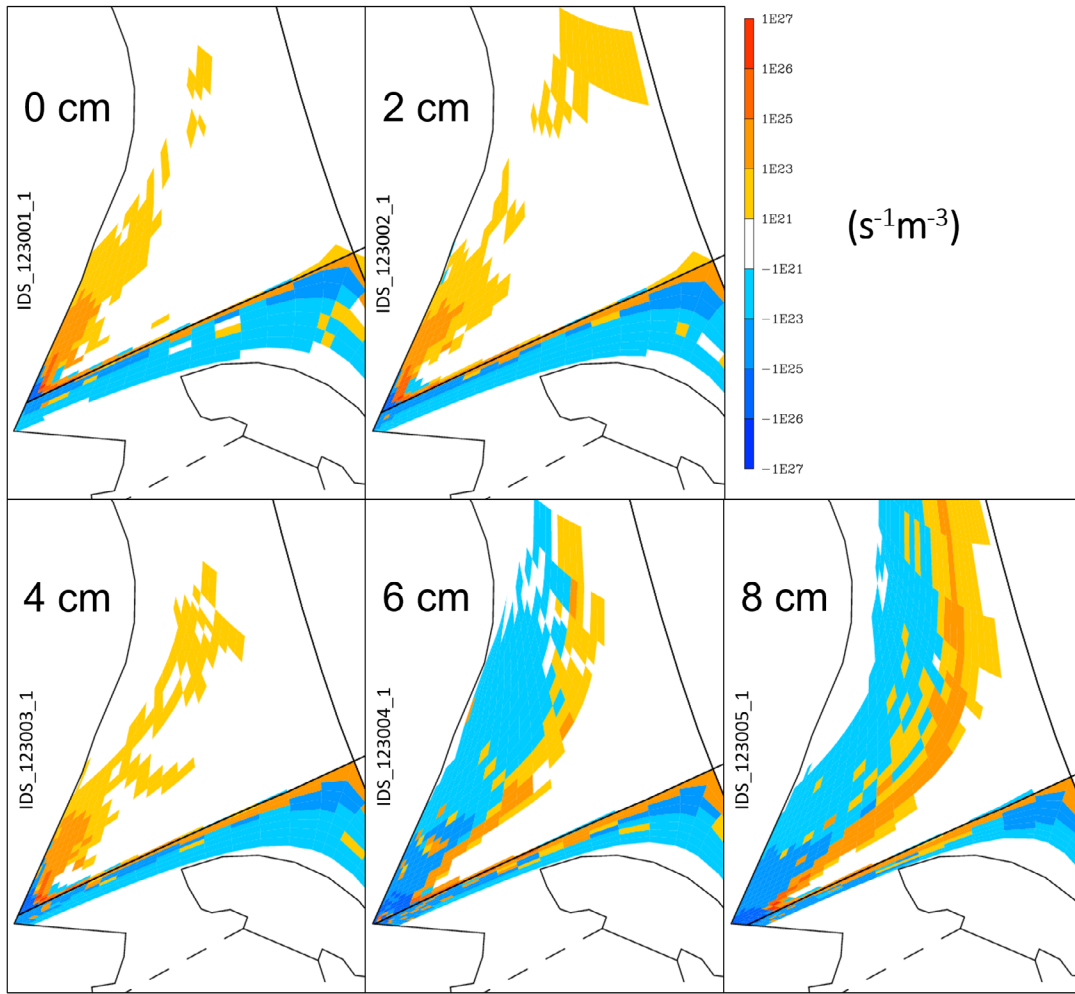


**Figure 27.** Distribution of the plasma particle source density at the inboard divertor for the different displacements. Negative particle source corresponds to recombining and positive to ionising plasma.

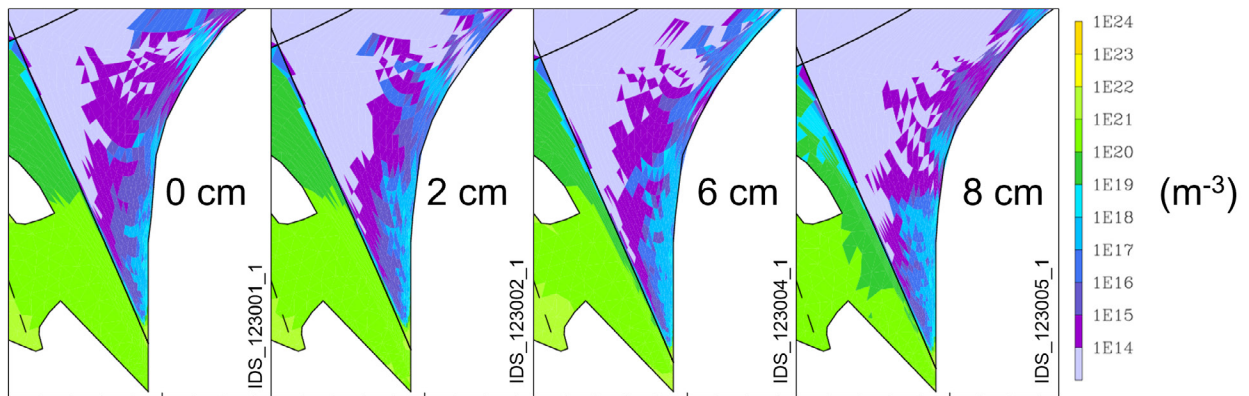


**Figure 28.** Distribution of neutral particle density (D atoms + D<sub>2</sub> molecules) at the OVT for the different displacements.

collision frequency for the neutral–neutral interactions within the divertor region is of  $\sim 10^5\text{--}10^6\text{ s}^{-1}$ , the same order of magnitude as the estimated frequency for CX and ionisation. Such effects have been noted in earlier ITER divertor design studies examining the impact of varying divertor geometry [13].

#### 4.2. Surface temperature calculations

To complete this Section, we make use of the new simplified heat transfer model developed here for SOLPS-ITER and described in section 3 to assess the surface temperatures to be expected on the divertor target surfaces as the strike point is

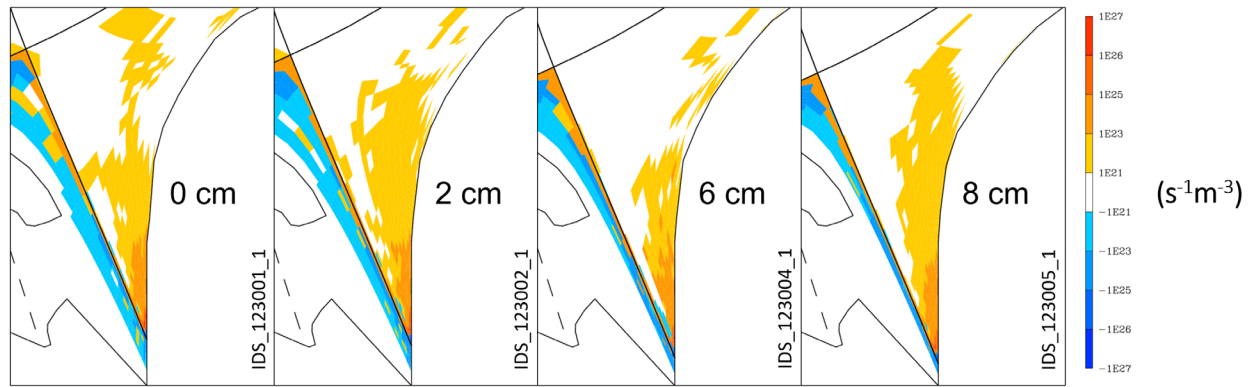


**Figure 29.** Distribution of particle source density at the OVT for the different displacements. Negative particle source corresponds to recombining and positive to ionising plasma.

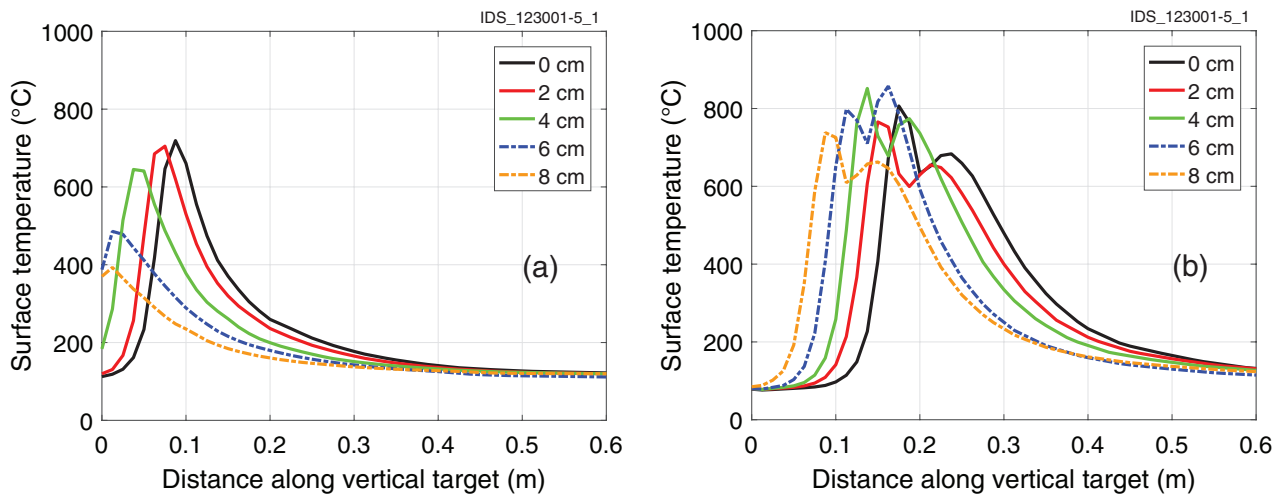


**Figure 30.** Profiles of peak surface temperature on (a) the inboard and (b) the outboard VTs, as a function of the distance along the wall from the V corner.

displaced. The thermal calculation is rapid, requiring  $\sim 10$  min on an Intel Core i7-6820HK for a single plasma scenario. Results for the poloidal profiles of the peak temperature computed on each 2D cross-section are compiled in figures 30 and 31 for the VT and RP surfaces respectively. Since there is no thermal coupling assumed between poloidally neighbouring tiles, the surface temperature profiles closely follow the corresponding heat flux density profiles (figure 11). Note that in the case of the VT monoblocks, which are toroidally bevelled for leading edge protection between toroidally neighbouring components, the temperature is highest at the highest point of the bevelled surface due to the increased power load there (figure 8(a)), where the total heat load comprises both thermal plasma and neutral/photonic power loading (see also [28]). There is, in addition, a toroidal variation in the surface temperature due to the cooling geometry (circular cooling channel within a rectangular block) which further raises the temperature at the upper right hand corner in figure 8(a). At the RPs, the absence of toroidal shaping and a much more uniform cooling provided by the hypervapotron channel makes for a symmetric top surface temperature distribution (figure 8(b)).

As a consequence of the reasonably detached reference condition chosen for these simulations, the peak VT surface temperatures remain well within required operational levels,

set by the requirement to remain always below tungsten recrystallization for stationary loading [42]. This value will be somewhere in the vicinity of  $1200\text{ }^{\circ}\text{C}$ , depending on variations within the batches of ITER grade tungsten which will be used to manufacture the divertor PFCs [42]. Surface temperatures on the RPs remain, as expected due to the lower power flux densities, far from any recrystallization limit. Even for the two cases in which the inner strike point accesses the IRP, the peak power flux density (and thus the corresponding surface temperature) remains relatively low as a consequence of the beneficial impact of the increased detachment degree for the horizontal configurations and the reduced angle of incidence on the plate, which further decreases the thermal plasma contribution compared with the vertical target condition. The outlet coolant temperature of the ORP in the worst-case scenario (the one with largest displacement) is  $\sim 110\text{ }^{\circ}\text{C}$  and has been compared to the saturation temperature to prove that boiling of coolant is avoided. Since no pressure loss calculation is performed within the simplified heat transfer model, the design outlet pressure of 26 bar is adopted as reference, yielding a saturation temperature of  $\sim 226\text{ }^{\circ}\text{C}$ , far from the computed outlet temperature. Interestingly, the maximum surface temperature values of  $\sim 550\text{ }^{\circ}\text{C}$  reached on the IRP for the 8 cm displacement may be of use for de-tritiation if it turns

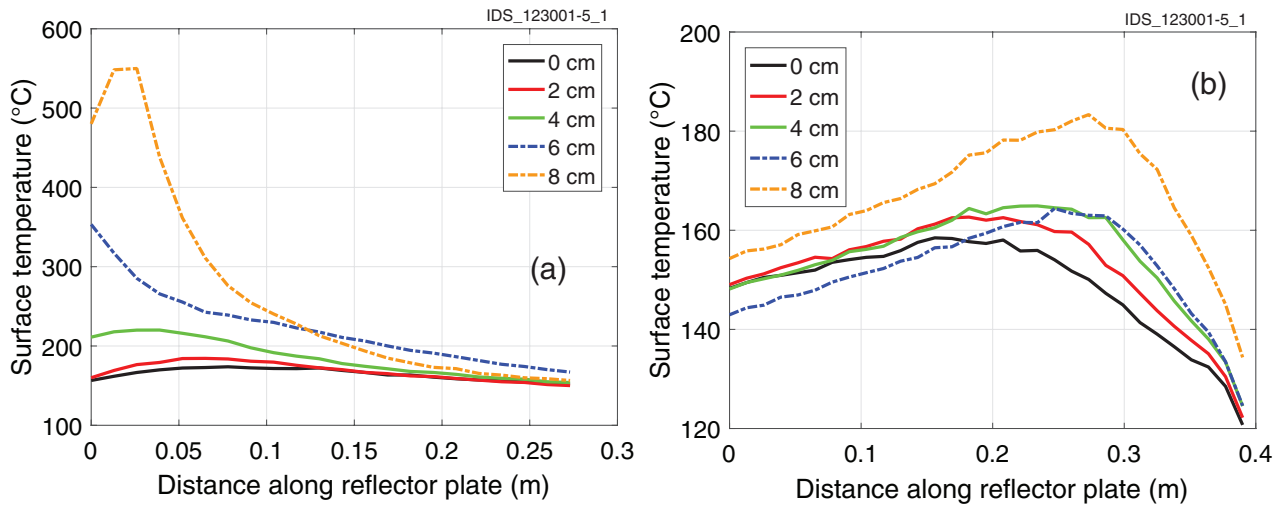


**Figure 31.** Profiles of peak surface temperature on (a) the inboard and (b) the outboard RPs, as a function of the distance along the wall from the left edge of each RP.

out that beryllium layers (due to migration of eroded main chamber material) do tend to grow at the inner target PFR and onto the IRP. Fuel co-deposited with this beryllium should be relatively easily desorbed at temperatures of several 100 °C and it may thus be that the downward vertical strike point displacements analysed here in the context of allowable target power loading may also be deliberately invoked as a detritiation method should fuel really be observed to accumulate on the inner RP.

## 5. Conclusions

The ITER divertor plasma performance has been studied for the first time in conditions in which magnetic equilibrium displacements place the strike points near or onto the divertor reflector plates as a consequence of an off-normal transient or as the result of a deliberate requirement. The SOLPS-ITER code in its coupled fluid plasma-kinetic neutral version has been adopted to perform a parametric study in which a baseline ITER scenario at  $Q_{DT} = 10$  and partially detached divertor conditions has been used as a starting point to obtain, through rigid downward equilibrium displacements, a series of steady-state solutions with different strike point positions up to the limit at which the inner dome wing intercepts the inboard divertor leg separatrix. The inner strike point falls on the reflector plate well before this limit while the outer strike point always remains on the vertical target.

As long as the inner strike point remains on the vertical target, there is no significant modification of the detachment character, with the plasma profiles and heat loading simply shifted downwards. When the strike point falls on the inner reflector plate, however, the target configuration switches from vertical to horizontal and the detachment is strongly enhanced, spreading the plasma power load by reducing the peak value by  $\sim 40\%$ , from  $\sim 7.5 \text{ MW m}^{-2}$  to  $\sim 4.4 \text{ MW m}^{-2}$ , and broadening the profile. The latter is due to an increased contribution from radiation in the PFR while the peak reduction is a consequence of the neutral recycling being now

mainly directed towards the SOL region and not the separatrix. This strongly modifies the neutral distribution within the inboard divertor, reduces the plasma particle flux on the walls and in turn the plasma heat flux on the surface. For the most downwards displaced case, corresponding to the largest excursion of the inner strike point onto the reflector plate, the neutral pressure in the inboard PFR below the dome is significantly reduced and the pumping rate is reduced to 50% of the reference vertical target configuration. However, the He ash removal capability does not seem to be compromised, with the separatrix He density largely unaffected. On the outboard divertor, where the strike point moves down on the target but never reaches the outer reflector plate, the divertor plasma remains essentially invariant with increasing displacement (as is also the case for the inner divertor as long as the strike point remains on the vertical target). These observations can be taken as a qualitative indication of the importance of the strong neutral-neutral interactions in the ITER divertor at high performance.

The heat loading condition on the reflector plates is largely driven by photonic radiation from the divertor plasma above, as found in previous studies with fixed vertical target strike points. When the strike point accesses the reflector plate, the loads increase considerably, as expected, due to the added thermal plasma component, but the stronger detachment obtained in the horizontal target configuration, together with the reduced incidence angles, yields much lower peak heat flux densities than would be obtained if the vertical target loads were assumed to be preserved (as has been assumed in simple, conservative engineering heat load studies to date).

The results of this study are, in common with all predictive simulations for ITER, dependent on the strength of radial heat transport which determines the power decay length  $\lambda_q$ . As shown in [6], if  $\lambda_q$  were to be reduced further below the  $\sim 2 \text{ mm}$  value adopted in this study (through the choice of lower perpendicular heat diffusivity), the power dissipated through radiation (mainly from impurities) in the near SOL would increase, driven by the increased density. Partially detached conditions can thus still be achieved and similar heat

flux densities can be reached on the targets, albeit at the price of higher upstream density.

A simplified 2D finite element heat transfer model, successfully benchmarked against a 3D ANSYS model in the case of the vertical target monoblocks, has been developed here for the ITER divertor components and is now included in the SOLPS-ITER code suite. It permits a rapid estimation of the thermal response of the vertical targets and reflector plates (each using different cooling techniques) under different operating scenarios and now allows routine estimates for the vertical plate surface temperature distributions from within the SOLPS-ITER code, without recourse to the more complex and time-consuming 3D simulations typically used in engineering studies. For the heat loading conditions driven by the partially detached plasma scenarios in this study, the maximum tungsten temperature remains below the recrystallization threshold both on the vertical targets and reflector plates. A large (~8 cm) downward displacement might be useful for de-tritiation, in case fuel co-deposition on the inner target PFR and IRP is confirmed, as, for the conditions in our study, the induced tungsten temperatures are in the desorption range.

## Acknowledgments

The views and opinions expressed herein do not necessarily reflect those of the ITER Organization. ITER is the nuclear facility INB 174.

The study reported in this paper was started when the first author, at that time a PhD student in the NEMO group at the Politecnico di Torino, was seconded to the ITER International Organization, before he moved to his current position at KU Leuven, where the work was completed.

## ORCID iDs

S. Carli  <https://orcid.org/0000-0001-6581-2745>  
 R.A. Pitts  <https://orcid.org/0000-0001-9455-2698>  
 F. Subba  <https://orcid.org/0000-0002-8170-4792>  
 R. Zanino  <https://orcid.org/0000-0003-0334-8275>

## References

- [1] Pitts R.A. et al 2013 *J. Nucl. Mater.* **438** S48–56
- [2] Kukushkin A.S., Pacher H.D., Kotov V., Reiter D., Coster D. and Pacher G.W. 2005 *Nucl. Fusion* **45** 608
- [3] Kukushkin A.S., Pacher H.D., Loarte A., Komarov V., Kotov V., Merola M., Pacher G.W. and Reiter D. 2009 *Nucl. Fusion* **49** 075008
- [4] Kukushkin A.S., Pacher H.D., Kotov V., Reiter D., Coster D.P. and Pacher G.W. 2007 *J. Nucl. Mater.* **363–5** 308–13
- [5] Pacher H.D., Kukushkin A.S., Pacher G.W., Kotov V. and Reiter D. 2011 *J. Nucl. Mater.* **415** S492–6
- [6] Kukushkin A.S., Pacher H.D., Pacher G.W., Kotov V., Pitts R.A. and Reiter D. 2013 *J. Nucl. Mater.* **438** S203–7
- [7] Kukushkin A.S. and Pacher H.D. 2016 *Nucl. Fusion* **56** 126012
- [8] Hirai T. et al 2018 *Fusion Eng. Des.* **127** 66–72
- [9] Escourbiac F., Schlosser J., Merola M. and Bobin Vastra I. 2003 *Fusion Eng. Des.* **66–8** 301–4
- [10] Pacher H.D., Kukushkin A.S., Pacher G.W., Kotov V., Pitts R.A. and Reiter D. 2015 *J. Nucl. Mater.* **463** 591–5
- [11] Kukushkin A.S., Pacher H.D., Kotov V., Pacher G.W., Pitts R.A. and Reiter D. 2013 *Nucl. Fusion* **56** 123025
- [12] Guillemaut A., Pitts R.A., Kukushkin A.S. and O’Mullane M. 2011 *Fusion Eng. Des.* **86** 2954–64
- [13] Kukushkin A.S., Pacher H.D., Kotov V., Reiter D., Coster D. and Pacher G.W. 2007 *Nucl. Fusion* **47** 698
- [14] Loarte A. 2001 *Plasma Phys. Control. Fusion* **43** R18
- [15] Wiesen S. et al 2015 *J. Nucl. Mater.* **463** 480–4
- [16] Bonnin X., Dekeyser W., Pitts R.A., Coster D., Voskoboinikov S. and Wiesen S. 2016 *Plasma Fusion Res.* **11** 1403102
- [17] Bonnin X., Kukushkin A.S. and Coster D. 2009 *J. Nucl. Mater.* **390–1** 274–7
- [18] Coster D.P. 2016 *Contrib. Plasma Phys.* **56** 790–5
- [19] ITER Physics Basis 1999 *Nucl. Fusion* **39** 2175
- [20] Eckstein W. 2007 *Sputtering by Particle Bombardment* (Berlin: Springer)
- [21] Kotov V., Reiter D., Pitts R.A., Jachmich S., Huber A., Coster D. and JET-EFDA Contributors 2008 *Plasma Phys. Control. Fusion* **50** 105012
- [22] Sieglin B. et al 2013 *Plasma Phys. Control. Fusion* **55** 124039
- [23] Chang C.S. et al 2017 *Nucl. Fusion* **57** 116023
- [24] Eckstein W. 1991 *Computer Simulation of Ion-Solid Interactions* (Berlin: Springer)
- [25] Kukushkin A.S., Pacher H.D., Kotov V., Pacher G.W. and Reiter D. 2011 *Fusion Eng. Des.* **86** 2865–73
- [26] Summers H.P. 1994 *Atomic Data and Analysis Structure Users Manual, JET-IR 06* (Abingdon: JET Joint Undertaking)
- [27] Imbeaux F. 2015 *Nucl. Fusion* **55** 123006
- [28] Pitts R.A. et al 2017 *Nucl. Mater. Energy* **12** 60–74
- [29] Gunn J.P., Carpentier-Chouchana S., Escourbiac F., Hirai T., Panayotis S., Pitts R.A., Corre Y., Dejarnac R., Firdaouss M. and Kočan M. 2017 *Nucl. Fusion* **57** 046025
- [30] Carpentier-Chouchana S. et al 2014 *Phys. Scr.* **T159** 014002
- [31] Hirai T. et al 2017 *Phys. Scr.* **T170** 014045
- [32] Hecht F. 2012 *J. Numer. Math.* **20** 251–65
- [33] Savoldi L., Casella F., Fiori B. and Zanino R. 2010 *Cryogenics* **50** 167–76
- [34] Marshall T.D., Youchison D.L. and Cadwallder L.C. 2001 *Fusion Technol.* **39** 849–55
- [35] [www.ansys.com](http://www.ansys.com) (Accessed: 1 August 2018)
- [36] Pitts R.A. et al 2018 *Nucl. Mater. Energy* submitted
- [37] Kaveeva E. et al 2018 private communication
- [38] Pitts R.A. et al 2005 *J. Nucl. Mater.* **337–9** 146–53
- [39] Jaervinen A.E. et al 2016 *Plasma Phys. Control. Fusion* **58** 0450141
- [40] Merola M. et al 2010 *Fusion Eng. Des.* **85** 2312–22
- [41] Carralero D. et al 2017 *Nucl. Fusion* **57** 056044
- [42] De Temmerman G., Hirai T. and Pitts R.A. 2018 *Plasma Phys. Control. Fusion* **60** 044018